Faculty of Physics and Astronomy
Heidelberg University

Bachelor Thesis

in Physics

submitted by

Joyce Nicole Louisa Glass

born in Cologne

2022

Evaluating a novel microstructured, superconducting resonator for the analysis of dielectric properties of N-BK7 at 1 GHz and low temperatures

This Bachelor Thesis was conducted by Joyce Nicole Louisa Glass
at the Kirchhoff-Institut for Physics
under the supervision of
Prof. Dr. C. Enss

In this thesis a novel microstructured, superconducting resonator is tested to see if it can be used to analyse the borosilicate glass N-BK7 through dielectric measurements at a resonance frequency of 1 GHz and at low temperatures. The Standard Tunneling Model and previous measurements conducted on N-BK7 are used to assess the obtained results. Equilibrium measurements are conducted which include the measurement of the temperature dependency in the range of 10^{-2} K to 1 K and the power dependency in the range of -115 dBm to -65 dBm of the sample. The temperature dependency measurements show some deviation to the theory but a good agreement with previous results obtained by a different resonator. The power dependency measurements show the expected behaviour but could not be successfully described by a fit function. The non-equilibrium measurements include Landau-Zener spectroscopy which is implemented with an additional electric bias field. The bias rate was applied by a triangle signal which was varied by either changing the frequency or the voltage of the signal. The frequency dependent measurements show a good agreement to the expected behaviour. The voltage dependent measurements show deviating behaviour which led to a further measurement to ensure that no external heating effects were responsible.

Evaluation eines neuen mikrostrukturierten, supraleitenden Resonators für die Analyse der dielektrischen Eigenschaften von N-BK7 bei 1 GHz und niedrigen Temperaturen

In dieser Arbeit wird ein mikrostrukturierter, supraleitender Resonator getestet um die Eignung für die Analyse von dem Borosilikatglas N-BK7 durch dielektrische Messungen bei einer Resonanzfrequenz von 1 GHz und bei niedrigen Temperaturen zu überprüfen. Die Ergebnisse werden mithilfe des Standardtunnelmodels und früherer Messungen evaluiert. Es werden Gleichgewichtsmessungen an N-BK7 durchgeführt, die die Messung der Temperaturabhängigkeit im Bereich von 10^{-2} K bis 1 K und der Leistungsabhängigkeit im Bereich von -115 dBm bis -65 dBm beinhalten. Die Temperaturabhängigkeitsmessungen zeigen teilweise Abweichungen zur Theorie aber eine gute Übereinstmmung zu vergangenen Messungen mit einem anderen Resonator. Die Leistungsabhängigkeitsmessungen zeigen den erwarteten Verlauf, konnten aber nicht erfolgreich mithilfe einer Fitfunktion beschrieben werden. Die Nicht-Gleichgewichtsmessungen beinhalten Messungen mit Landau-Zener Dynamik. Diese wird mithilfe eines elektrischen Vorspannungsfeldes realisiert, das durch ein Dreieckssignal angelegt wird. Das elektrische Vorspannungsfeld wird variiert, indem entweder die Frequenz oder die Spannungsamplitude des Signals verändert wird. Die frequenzabhängige Messung zeigt eine gute Übereinstimmung zum erwarteten Verlauf. Die spannungsabhängige Messung zeigt ein abweichendes Verhalten zur Theorie, weswegen Heizeffektmessungen durchgeführt werden, um zu versichern, dass kein zusätzliches Heizen für das Verhalten verantwortlich ist.

Contents

1. Introduction

Crystals have a short- and long-range periodicity which allow a good understanding of their inner workings. The periodic structure enables a description of crystals with the help of phonons that are interpreted as elementary excitations of the lattice [Hun18]. In contrast, amorphous solids do not posses a long-range periodicity because their bonding angles vary statistically [Ell84]. This makes it more difficult to describe them theoretically. A model that has so far described amorphous solids fairly well is the Standard Tunneling Model (STM) which was independently worked out by [And72] and [Phi72]. It describes the characteristics of the material by assuming that it originates from two-level atomic tunneling systems. The STM is able to account for the differences of the thermal properties between crystals and amorphous solids, which were first observed by [Zel71], due to the interaction of the tunneling systems with phonons. The model also provides a good description for dielectric measurements [Fre21], and ultrasonic absorption [Hun72, vS77]. However, the model fails to provide a microscopical origin for the observed phenomena. Further, the model is not always able to fully describe the experimental observations.
As a result, different additions have been made to the STM over time. One such addition is the incorporation of interactions between tunneling systems [Bur95, Nal04] which gains importance in the low temperature regime.
As the additions show, the understanding of the inner workings of the amorphous solids need to be improved even further. This can be experimentally done by studying the reactions of the amorphous solids to external stimuli like electric probe- and bias fields. Recently, the usage of Landau-Zener transitions as a way to study amorphous thin films was introduced by [Kha14] and has already been applied to amorphous solids by [Fre21]. In such experiments an electric bias field is used to control the energy splittings of the tunneling systems to suppress the saturation of the dielectric loss.
In order to do this the proper tools are needed that are able to produce these external stimuli but also ensure a good measurement of the solid's reaction. Currently, a Wheatstone-bridge setup is used [Lut18, Kö19, Lut20, Fre21]. This setup contains multiple capacitors which makes it harder to build. The goal of this thesis is it to test a new resonator setup that only contains one capacitor per resonator, thus, is easier to build and therefore prone to less non-linearities. Because of the simpler setup it is also easier to describe in terms of it's electronic features.
The experiments conducted in this thesis will determine if the expected behaviour of the amorphous solid can be reproduced. The expected behaviour is given by the theoretical expectation and previous experimental observations.

The thesis at hand is divided into five components. In Chapter 2 the theory needed for the understanding of the experiments is introduced. The theory includes current knowledge on amorphous solids at low temperatures, the description of the STM and various effects that arise when amorphous solids are being influenced by an electric probe- or bias field. After being equipped with the necessary knowledge, the experimental methods are depicted in Chapter 3. Here the chosen sample, the pathway of the electric signal, and, of course, the resonator are introduced. The thesis continues with Chapter 4 which depicts the individual experiments, the measurement results and the corresponding analysis of the results. Here, equilibrium measurements, such as the power- and temperature dependency measurements are conducted, as well as, non-equilibrium measurements in form of the Landau-Zener Spectroscopy measurements. Lastly, a conclusion and future outlook will be provided in Chapter 5.

2. Theory

In this chapter an introduction will be given on amorphous solids and the interactions that take place within them at very low temperatures while under the influence of different external impulses. First, the general properties of amorphous solids at low temperatures are introduced in Section 2.1. Next, the Standard Tunneling Model that theoretically describes amorphous systems is depicted in Section 2.2. Since the behaviour of the sample will be analysed under the influence of a constant probing field the dielectric function is introduced in Section 2.3. Sections 2.4 and 2.5 describe the resonant- and relaxation interaction, respectively. Those are the interactions that occur in amorphous solids while being probed by a constant electric field. The last Section 2.6 theoretically describes the behaviour of an amorphous solid under the influence of an additional electric bias field.

2.1 Low Temperature properties of amorphous solids

There are some fundamental differences between crystals and amorphous solids which are rooted in the different structural periodicity of the two solids as depicted in Figure 2.1.

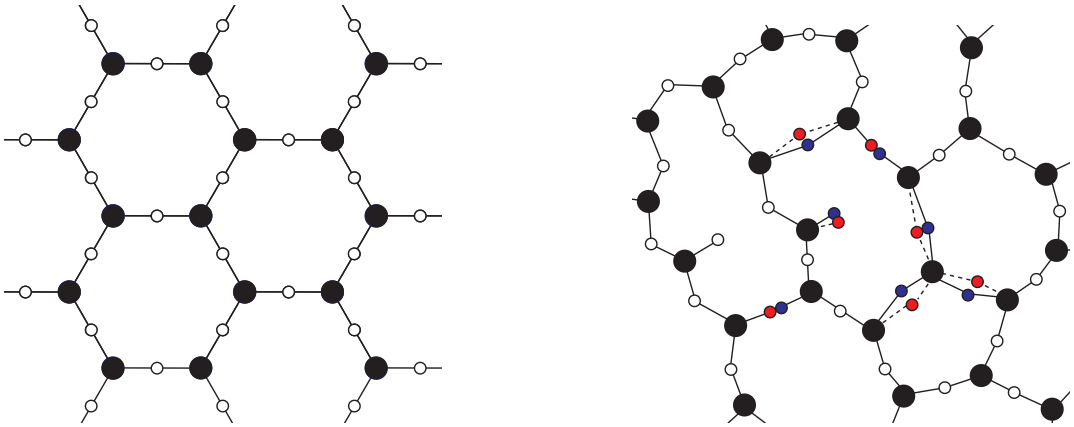

Figure 2.1: Schematic drawing of the crystalline- (left) and the amorphous structure (right). In the amorphous solid some atoms are able to transition between two energetically identical positions as indicated by the red and blue dots [Zac32, Hun74, Mü21].

While crystals are periodic in every aspect, amorphous solids only have have a short- but no long-range order. Meaning that their bonding angles and bonding lengths can vary [Hun74]. This leads to different phenomena among which is a greater specific

heat and a decreased heat conductivity at low temperatures in comparison to crystals [Zel71]. In order to understand this, one has to take a closer look at the structure of the solid. As shown on the right in Figure 2.1 some atoms in amorphous solids can occupy multiple positions which are almost energetically identical.
To describe this configuration a microscopic description through two-level systems as seen in Figure 2.2 is used. These can be interpreted as a superposition of two double-well potentials with a potential barrier of height V between them. The possible positions that can be occupied by an atom can be described with the distance d between them, the asymmetry energy Δ which is related to the environment around the particle and the ground state energy $\hbar\Omega/2$. Ω denotes the angular frequency of the oscillator and $\hbar$ is the Planck constant divided by 2π.

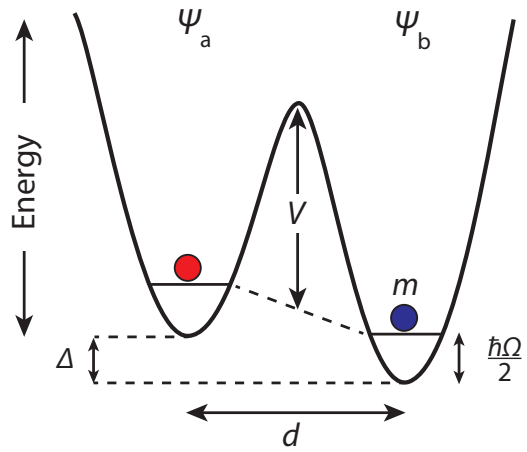

Figure 2.2: Schematic drawing of a double well potential as a superposition of two harmonic potentials with ground state energy $\hbar\Omega/2$, distance d, asymmetry energy Δ and potential barrier height V which can be tunneled through by the particle of mass m at low temperatures. Adapted from [Mü21, Phi81].

At higher temperatures for which $k_\mathrm{B}T \gg \Delta$ holds true, where k_B is the Boltzmann constant and T the temperature, the particle can overcome the barrier. However, at low temperatures this is only possible if the particle tunnels through the barrier since $k_\mathrm{B}T < \Delta$ holds for the thermal energy.
As lower temperatures are approached, the number of phonons decreases. This results in a decreased occupation of higher energy states. For $T < 1\,\mathrm{K}$ a tunneling system can resonantly absorb one phonon in order to enter the excited state. The tunneling system can then relax back into the ground state after the relaxation time τ. Because of this the thermal conductivity is lower in comparison to crystals.
When an electric field is applied it couples to the tunneling system through a permanent dipole moment. The thermal equilibrium of the two-level system can then be disturbed by an electromagnetic wave. After a system is disturbed, it takes the

relaxation time τ to relax back into its thermal equilibrium. This process is accompanied by the emission or absorption of thermal photons.
Another difference in comparison to crystals is that the ultrasonic absorption increases in amorphous solids for low temperatures [Hun72]. This is because the tunneling systems resonantly interact with the sonic waves. In order for a resonant interaction to occur, the energy of the sonic phonon has to match the energy splitting E of the tunneling system. If this condition is given, a phonon can be either absorbed or emitted depending on the occupation of the energy levels. At very low temperatures where $k_\mathrm{B}T \ll E$ almost all particles occupy the ground state which means that phonons can only be absorbed. For $k_\mathrm{B}T \gg E$ on the other hand the ground- and excited state are approximately occupied by the same number of particles meaning that the resonant interaction occurs roughly at the same rate for either the absorption or emission of a phonon.
Since the rate of ultrasonic absorption is dependent on which state the tunneling system is occupying, the population difference between the two energy levels is introduced as [Ens05]

$$\Delta n = n_2 - n_1 = n \tanh\left(\frac{E}{2k_\mathrm{B}T}\right) \tag{2.1}$$

with n_1 and n_2 being the density of tunneling systems in the ground- or the excited state respectively and n is the total number of available two-level systems.
Further, it is known that the mean free path is limited by the resonant interaction between phonons and tunneling systems and can be written as [Hun76]

$$l_\mathrm{res}^{-1} = l_0^{-1} \frac{\tanh\left(\frac{\hbar\omega}{2k_\mathrm{B}T}\right)}{(1 + J/J_\mathrm{c})^{1/2}}. \tag{2.2}$$

J_c is used to denote the critical acoustic intensity, ω is the angular frequency of the applied signal, l_0^{-1} is the inverse mean free path at $T = 0\,\mathrm{K}$ and at an acoustic intensity approaching zero. For low temperatures the population difference can be approximated to $\Delta n \approx n$, since almost all tunneling systems are in the ground state. This means that the mean free path is almost temperature independent. For higher temperatures $\Delta n \approx nE/2k_\mathrm{B}T$ which indicates a frequency and temperature dependency. Because the occupation of the excited state increases with the sonic intensity J the damping through resonant processes will decrease and the dielectric loss, denoted as $\tan\delta$, will saturate.
Similarly, the dielectric loss problem was solved by [vS77] by using

$$\tan\delta = \tan\delta_0 \frac{\tanh\left(\frac{\hbar\omega}{2k_\mathrm{B}T}\right)}{\sqrt{1 + |\mathbf{F}|^2/F_\mathrm{c}^2}} \tag{2.3}$$

to describe the dielectric loss in response to an applied electric field **F** with a critical electric field F_c.

2.2 Standard Tunneling Model

The Standard Tunneling model was introduced in 1972 independently by [And72] and [Phi72] to describe the low temperature phenomena in amorphous solids. The theory is based on the assumption that some atoms have the ability to occupy multiple positions in amorphous solids. It has already been mentioned that a particle that can occupy two energetically almost equivalent positions can be described through a two-level system with a potential consisting of two harmonic wells. Now a more detailed depiction of this theory will follow.

2.2.1 Two-level systems

In the following the theory of two-level systems, which can be seen in Figure 2.2, will be mathematically described.
The wave function of a two-level system is a linear combination of the two wave functions Ψ_a and Ψ_b with their corresponding complex coefficients a and b,

$$\Psi = a\Psi_a + b\Psi_b \tag{2.4}$$

representing two individual harmonic oscillators as depicted in Figure 2.2.
In order to find the energy eigenvalue E of such a system the time-independent Schrödinger-equation

$$H\Psi = E\Psi \tag{2.5}$$

needs to be solved with

$$E \leq \frac{\langle\Psi|H|\Psi\rangle}{\langle\Psi|\Psi\rangle} = \frac{a^2E_{aa} + b^2E_{bb} + 2abE_{ab}}{a^2 + b^2 + 2abS} \tag{2.6}$$

for which the equations

$$\begin{aligned} E_{ii} &= \langle\Psi_i \,|\, H \,|\, \Psi_i\rangle \qquad \text{with} \quad i \in \{a, b\}, \\ E_{ab} &= \langle\Psi_a \,|\, H \,|\, \Psi_b\rangle \qquad \text{and} \\ S &= \langle\Psi_a \,|\, \Psi_b\rangle \end{aligned}$$

were used. E_{ii} are the corresponding eigenvalues of the particle in the isolated well, E_{ab} expresses the exchange energy and S is the overlap of the two wave functions. The true wave function in the ground state will minimize E. Hence the requirement

$\partial E/\partial a = \partial E/\partial b = 0$ is implemented. With this we find

$$(E_{\mathrm{aa}} - E)(E_{\mathrm{bb}} - E) - (E_{\mathrm{ab}} - ES)^2 = 0. \tag{2.7}$$

If the ground state energy is defined as being between the two potential minima, the energy eigenvalue of the particle in the isolated wells becomes

$$E_{\mathrm{aa}} = \frac{\hbar\Omega + \Delta}{2}, \tag{2.8}$$

$$E_{\mathrm{bb}} = \frac{\hbar\Omega - \Delta}{2}. \tag{2.9}$$

Under the assumption that the overlap of the wave functions is weak, the term $E \cdot S$ can be neglected. Furthermore, the interaction energy can be approximated by the WKB[1]-method as

$$\Delta_0 = -2E_{\mathrm{ab}} \approx \hbar\Omega e^{-\lambda} \tag{2.10}$$

with λ being the tunneling parameter

$$\lambda \approx \frac{d}{2\hbar}\sqrt{2mV} \tag{2.11}$$

which is dependent on the mass m of the particle and the potential barrier height V of the tunneling system. Given this information, equation (2.7) can be transformed to

$$\left(\frac{\hbar\Omega}{2} + \frac{\Delta}{2} - E\right)\left(\frac{\hbar\Omega}{2} - \frac{\Delta}{2} - E\right) + \frac{\Delta_0}{2} = 0. \tag{2.12}$$

From this equation the energy eigenvalues

$$E_{\pm} = \frac{1}{2}\left(\hbar\Omega \pm \sqrt{\Delta^2 + \Delta_0^2}\right) \tag{2.13}$$

are obtained. The resulting wave functions Ψ_+ and Ψ_- represent the ground- and first excited state and can be thereby named the symmetric and antisymmetric wave functions, respectively and can be seen in Figure 2.3.
The energy-splitting of the ground state can be now calculated as

$$E = E_+ - E_- = \sqrt{\Delta^2 + \Delta_0^2}. \tag{2.14}$$

[1]Wentzel-Kramers-Brillouin

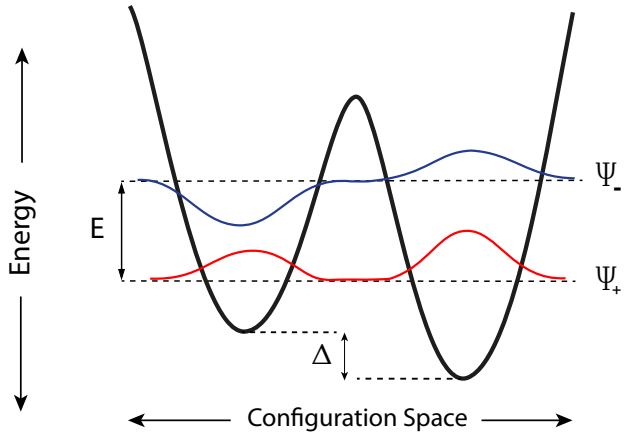

Figure 2.3: Superposition of the wave function of the ground state Ψ_+ and of the excited state Ψ_- of a tunneling system with the asymmetry energy Δ and the energy splitting E. Adapted from [Fre16].

2.2.2 Coupling between two-level systems and electric fields

When an electric field is applied, the environment of the particle changes. This in turn also changes the asymmetry energy Δ of the two-level system. In case of small enough electric fields the coupling can be described by first order perturbation theory [Ens05]. The total Hamiltonian changes to

$$H = H_0 + H_\mathrm{S}, \tag{2.15}$$

where H_S is the perturbed Hamiltonian due to the field and H_0 is the Hamiltonian of the two-level system without any perturbation. In the basis of the isolated wells $\Psi_{\mathrm{a,b}}$ the unperturbed Hamiltonian is

$$H_0 = \frac{\hbar\Omega}{2} + \frac{1}{2}\begin{pmatrix} \Delta & -\Delta_0 \\ -\Delta_0 & -\Delta \end{pmatrix}. \tag{2.16}$$

Since the two states $\Psi_{\mathrm{a,b}}$ are not eigenstates of the total system one needs to write the Hamiltonian in its eigenbasis $\Psi_{+,-}$. For this the transformation matrix

$$T = \frac{1}{E}\begin{pmatrix} \Delta & \Delta_0 \\ -\Delta_0 & \Delta \end{pmatrix} \tag{2.17}$$

is used. With the transformation matrix, the Hamiltonian in its eigenbasis is obtained as

$$H_\mathrm{TS} = \frac{\hbar\Omega}{2} + \frac{1}{2}\begin{pmatrix} E & 0 \\ 0 & -E \end{pmatrix} \tag{2.18}$$

in which E describes the energy-splitting of the ground state.
Looking at the Hamiltonian's off-diagonal elements one sees that in the unperturbed state no spontaneous transitions between the states Ψ_+ and Ψ_- are possible. However, tunneling systems can posses dipole moments $\boldsymbol{p}$ due to local charge distributions. If a tunneling system has a dipole moment it can interact with an external electric field $\boldsymbol{F}$. An electric field alters the environment of a particle and as a result the asymmetry energy Δ is altered. For a weak electric field and a linearly varying asymmetry energy we find

$$\delta\Delta = 2\boldsymbol{p}\boldsymbol{F} = 2pF\cos\theta. \tag{2.19}$$

Here θ is the angle between the dipole moment $\boldsymbol{p}$ and the applied electric field $\boldsymbol{F}$. Contrary to the asymmetry energy the impact on the tunnel splitting Δ_0 is negligible. This is because the distance between the potential minima and the barrier height remains mostly unaffected by the field. Thus, the tunnel splitting Δ_0 also remains approximately unchanged. As a result, the perturbation matrix reads

$$H_\mathrm{S} \approx \frac{1}{2}\begin{pmatrix} \delta\Delta & 0 \\ 0 & -\delta\Delta \end{pmatrix}. \tag{2.20}$$

Using once more the transformation matrix (2.17) on (2.20) the perturbation matrix in the eigenbasis of the tunneling system is obtained as

$$H_\mathrm{S} \approx \frac{1}{E}\begin{pmatrix} \Delta & -\Delta_0 \\ -\Delta_0 & -\Delta \end{pmatrix} p_0 F. \tag{2.21}$$

One can see from the diagonal elements that the external field modifies the energy splitting by

$$\delta E = \frac{2\Delta}{E} pF\cos\theta. \tag{2.22}$$

The off-diagonal elements give us an insight into the coupling and therefore the possible transitions between the states Ψ_+ and Ψ_-.

2.2.3 Distribution function

In order to explain macroscopic observations all tunneling systems of the solid need to be taken into account. Because their parameters vary statistically, their distribution function needs to be found. The STM assumes that the asymmetry energy Δ and the tunneling parameter λ can be considered independent from each other and are uniformly distributed. This results in a distribution function of the form

$$P(\Delta,\lambda)\, d\Delta d\lambda = P_0 d\Delta d\lambda \tag{2.23}$$

with the material dependent constant P_0. With a Jacobian transformation the following equation [Ens05]

$$P\left(E, \Delta_0\right) d\Delta_0 dE = P_0 \frac{E}{\Delta_0 \sqrt{E^2 - \Delta_0^2}} \tag{2.24}$$

can be found which is graphically depicted in Figure 2.4.

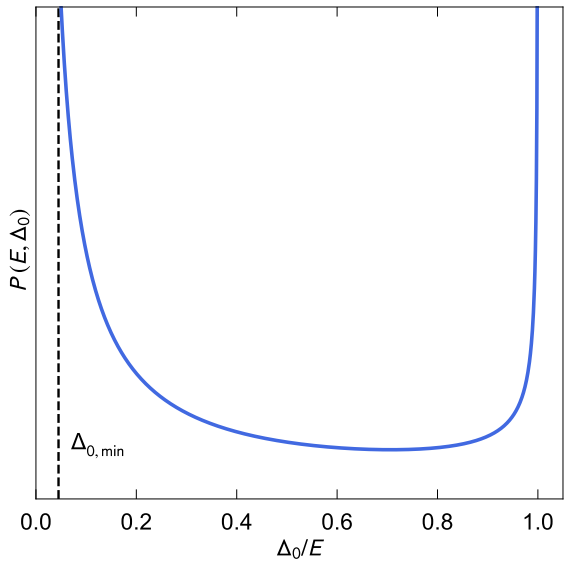

Figure 2.4: Distribution function $P(E, \Delta_0)$ plotted as a function of Δ_0/E. To avoid a nonphysical answer of infinite tunneling systems the parameter $\Delta_{0,\min}$ is introduced which denotes the minimal value the tunneling parameter Δ_0 can be.

It shows that two singularities occur at $\Delta_0 = 0$ and $\Delta_0 = E$ in the distribution function. In order to avoid a non-physical result for $\Delta_0 \to 0$ the minimum value $\Delta_{0,\min}$ has to be introduced. It is sensible to define $\Delta_{0,\min}$ dependent on the minimum temperature T_m that can be achieved within the experiment as it is done with the definition $\Delta_{0,\min} = 10^{-3} k_\mathrm{B} T_\mathrm{m}$ [Luc16].

2.3 Dielectric function

When an electric field acts on a dielectric material, charges will shift accordingly and form dipoles. The ability of a material to shift its charges in response to an electric field is called polarization

$$\boldsymbol{P} = \varepsilon_0 \chi \boldsymbol{F} \tag{2.25}$$

and it is dependent on the strength of the electric field $\boldsymbol{F}$, the permittivity in a vacuum ε_0 and the susceptibility χ. The susceptibility is material dependent and tells us how easily a given material can be polarized. Another important parameter is the dielectric function which is given as

$$\varepsilon = 1 + \chi. \tag{2.26}$$

If an oscillating electric field is applied the dielectric function will split into a real- and imaginary part

$$\varepsilon = \varepsilon' + i\varepsilon''. \tag{2.27}$$

Here the real part contains information about the energy that is stored in the material and the imaginary part represents the loss due to dissipation processes. The dielectric loss is defined as the ratio between real- and imaginary part

$$\tan\delta = \frac{\varepsilon''}{\varepsilon'} \tag{2.28}$$

and represents the dissipation factor with the loss angle δ.
Depending on the frequency range different polarization processes contribute to the dielectric function. The experiments conducted in the scope of this thesis take place in the GHz range in which orientation polarization outweighs the contribution due to electric- and ionic polarization [Hun18]. Therefore, it will be shortly discussed.
If a solid contains permanent dipoles the application of an electric field will alter the dipole moment because the potential energy

$$U = -\boldsymbol{pF} = -pF\cos\theta \tag{2.29}$$

is dependent on the angle θ between electric field and dipole moment. If a dipole has two equivalent positions available for occupation then its potential energy can be described by a two-level system. The electric field will lead to a difference in the energy according to equation (2.19) of the available energy-levels.
In case of a stationary electric field the polarization of a solid containing such dipoles follows the Langevin-Debye equation

$$P_0 = np\tanh\left(\frac{pF}{k_\mathrm{B}T}\right) \approx \frac{np^2F}{k_\mathrm{B}T}. \tag{2.30}$$

2.4 Relaxation effects

If one applies an electric field it is expected that the polarization exponentially grows as the time t progresses according to

$$P(t) = P_0\left(1 - \exp(-t/\tau)\right) \tag{2.31}$$

until reaching the new equilibrium polarization P_0. The relaxation time τ is dependent on the temperature range the experiment takes place in. For high temperatures the relaxation process is thermally activated. For low temperatures the particles can only overcome the potential barrier through tunnelling.

If an oscillating electric field is applied instead of a static one, the orientation of the dipoles and the energy splitting E will also change periodically. As a result, there will be a repeated reoccupation of the energy levels. Due to this continuous reoccupation, the dipoles are not in the equilibrium state and will try to relax back into it. For a periodically changing electric field the polarization and the equilibrium polarization change according to

$$P(t) = P(\omega)\exp(-i\omega t), \tag{2.32}$$

$$P_0(t) = P_0(0)\exp(-i\omega t). \tag{2.33}$$

By plugging the above equations into the relaxation equation, as was done in detail in [Hun18], we find

$$\frac{dP(t)}{dt} = -\frac{P(t) - P_0(t)}{\tau}. \tag{2.34}$$

By using the relation $P(\omega) = \varepsilon_0\chi(\omega)F(t)$, the susceptibility due to the dipoles can be written as

$$\chi_\mathrm{d}(\omega) = \frac{\chi_\mathrm{d}(0)}{1 - i\omega\tau}. \tag{2.35}$$

In order to find the dielectric function the contribution of the electric- and ionic polarization also has to be taken into account. The dielectric function then reads

$$\varepsilon(\omega) = 1 + \chi_\mathrm{i}(\omega) + \chi_\mathrm{e}(\omega) + \chi_\mathrm{d}(\omega). \tag{2.36}$$

Since the ionic- and electric contributions are constant in the GHz frequency range, as was mentioned previously, equation (2.36) can be rewritten and simplified to

$$\varepsilon(\omega) = 1 + \chi_\mathrm{i} + \chi_\mathrm{e} + \frac{\chi_\mathrm{d}(0)}{1 - i\omega\tau} = \varepsilon_\infty + \frac{\varepsilon_\mathrm{st} - \varepsilon_\infty}{1 - i\omega\tau}. \tag{2.37}$$

Here ε_∞ denotes the permittivity for high frequencies ($\omega\tau \gg 1$) and ε_st stands for the permittivity in the low frequency regime were $\omega\tau \ll 1$ holds. Differentiating between real- and imaginary part we find

$$\varepsilon'(\omega) = \varepsilon_\infty + \frac{\varepsilon_\mathrm{st} - \varepsilon_\infty}{1 + (\omega\tau)^2}, \tag{2.38}$$

$$\varepsilon''(\omega) = \frac{(\varepsilon_\mathrm{st} - \varepsilon_\infty)\,\omega\tau}{1 + (\omega\tau)^2}. \tag{2.39}$$

The behaviour of the real- and imaginary part can be seen in Figure 2.5. For $\omega\tau_1 \ll 1$ where the frequency of the field is small, one can observe that the dipoles can still follow the oscillating electric field, hence the real part of the dielectric function is large. For increasing frequencies the real part begins to decrease and experiences the

greatest decline at $\omega\tau_1 = 1$ at which point the imaginary part reaches its maximum value. For even higher frequencies $\omega\tau_1 \gg 1$ the dipoles are not able to follow the electric field anymore and they become quasi-static.

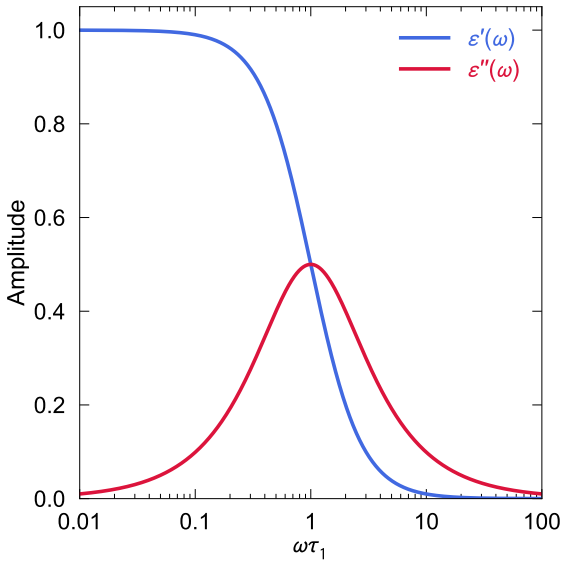

Figure 2.5: Real- ε' and imaginary part ε'' of the dielectric function as a function of $\omega\tau_1$ as a result of relaxation processes. τ_1 describes the relaxation time of a one-phonon process as introduced in equation (2.45).

Next, we want to find the change in the polarization and the dielectric function of the amorphous solid due to the electric field. When an external electric field is applied the alignment of the electric dipoles changes and therefore, a change in the energy splitting is induced. This leads to a change of the occupation number difference $\delta(\Delta n)$. As a result, we find with (2.1) and (2.25) the change in the polarization to be

$$\delta P = \delta(\Delta n)\frac{\Delta}{E}p\cos\theta. \tag{2.40}$$

In order to find $\chi_\mathrm{d}(0)$ from equation (2.37) the equations (2.1), (2.22), (2.25), and (2.40) are used to find

$$\chi_\mathrm{d}(0) = \frac{1}{\varepsilon_0}\frac{\partial P}{\partial F} = \frac{1}{\varepsilon_0}\frac{\partial(\delta P)}{\partial(\delta n)}\frac{\partial(\delta n)}{\partial(E)}\frac{\partial(E)}{\partial(F)} = \frac{p_0^2 N}{\varepsilon_0 k_\mathrm{B} T}\left(\frac{\Delta}{E}\right)^2 \mathrm{sech}^2\left(\frac{E}{2k_\mathrm{B}T}\right). \tag{2.41}$$

Thus, with equations (2.38) and (2.39) the change in permittivity can be found as

$$\delta\varepsilon'_\mathrm{rel} = \chi_\mathrm{d}(0)\frac{1}{1+(\omega\tau)^2}, \tag{2.42}$$

$$\delta\varepsilon''_\mathrm{rel} = \chi_\mathrm{d}(0)\frac{\omega\tau}{1+(\omega\tau)^2}. \tag{2.43}$$

2.4.1 Relaxation time

Now that we have seen what changes occur when an electric field is applied, we also want to have a look at the relaxation processes that lead to the relaxation of the amorphous solid back to its equilibrium state. The process implemented by the solid is dependent on the temperature regime it is experiencing.
For high temperatures relaxation occurs through thermally activated jumps for which many phonons are needed. Since the number of phonons decreases with decreasing temperature the tunneling system relaxes back to its equilibrium state through the Raman process, also known as two-phonon relaxation process at intermediate temperatures. This is because the potential barrier cannot be overcome classically anymore and the transitions occur between the split ground state and intermediate states that may be real or virtual. The two-phonon relaxation time reads [Dou80]

$$\tau_{2\mathrm{P}}^{-1} = R\left(\frac{\Delta_0}{E}\right)^2 T^7 f\left(\frac{E}{2k_\mathrm{B}T}\right) \tag{2.44}$$

and depends on the constant R that describes the coupling strength of the process and the function[2] f.
Lastly, at low temperatures for which $k_\mathrm{B}T \lesssim E$ is fulfilled, the relaxation process occurs through the one-phonon process where the transition is made through the absorption or emission of one thermal phonon. By calculating the transition probabilities through Fermi's golden rule, the inverse longitudinal relaxation time is found as [Jä72]

$$\tau_{1\mathrm{P}}^{-1} = \left(\frac{\Delta_0}{E}\right)\frac{E^3}{K_{1\mathrm{P}}}\coth\left(\frac{E}{2k_\mathrm{B}T}\right) \tag{2.45}$$

with the coupling constant

$$K_{1\mathrm{P}} = 2\pi\rho\hbar^4\left(\frac{\gamma_l^2}{\nu_\mathrm{l}^5} + 2\frac{\gamma_\mathrm{t}^2}{\nu_\mathrm{t}^5}\right)^{-1} \tag{2.46}$$

where ρ is the mass density, $\nu_{\mathrm{l,t}}$ are the sound velocities and $\gamma_{\mathrm{l,t}}$ the coupling strengths of the longitudinal and transversal phonons to the tunneling system.
The relaxation time becomes maximal for very asymmetric tunneling systems where Δ_0 is minimal. Consequently, the relaxation time is minimal for symmetric tunneling systems where $\Delta_0 = E$.
The total longitudinal relaxation time can then be approximated as

$$\tau^{-1} \approx \tau_{1\mathrm{P}}^{-1} + \tau_{2\mathrm{P}}^{-1} \tag{2.47}$$

[2] $f(x) = \frac{x}{70}\left(x^2+\pi^2\right)\left(x^4 - \pi^2x^2 + \frac{10}{3}\pi^4\right)\coth(x)$

if higher order phonon processes are neglected.

2.5 Resonant Interaction

Resonant interactions depict the interaction of the tunneling systems with the electric field through the absorption of photons. A photon from the electric field with the energy $\hbar\omega$ can be resonantly absorbed by a tunneling system with the resonant frequency ω_0 and the corresponding energy $E = \hbar\omega_0$, if their energies match. The resonant absorption excites the system from its ground into its excited state. As can be seen in Figure 2.6 the system absorbs photons the most efficient when $\omega = \omega_0$, resulting in the largest contribution to the imaginary part due to the high energy dissipation.

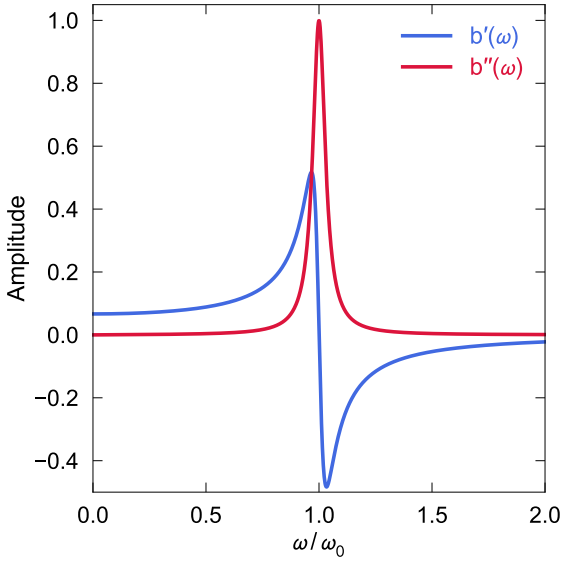

Figure 2.6: Frequency dependence of the real- $b'(\omega)$ and the imaginary part $b''(\omega)$ of the dielectric function as a function of ω/ω_0 as a result of resonant processes.

The real part receives contributions from tunneling systems of all frequencies ω and changes its sign at the resonance frequency. Through resonant processes the dielectric function changes according to [Fre21]

$$\delta\varepsilon'_{\mathrm{res}} = \frac{p_0^2}{\varepsilon_0\varepsilon_{\mathrm{r}}\hbar}\left(\frac{\Delta_0}{E}\right)^2 \tanh\left(\frac{E}{2k_{\mathrm{B}}T}\right) b'(\omega), \tag{2.48}$$

$$\delta\varepsilon''_{\mathrm{res}} = \frac{p_0^2}{\varepsilon_0\varepsilon_{\mathrm{r}}\hbar}\left(\frac{\Delta_0}{E}\right)^2 \tanh\left(\frac{E}{2k_{\mathrm{B}}T}\right) b''(\omega) \tag{2.49}$$

with the parameters

$$b'(\omega) = \left[-\frac{(\omega - \omega_0)}{(\omega - \omega_0)^2 \tau_2^2 + 1} + \frac{(\omega + \omega_0)}{(\omega + \omega_0)^2 \tau_2^2 + 1} \right] \tau_2^2, \tag{2.50}$$

$$b''(\omega) = \left[-\frac{1}{(\omega - \omega_0)^2 \tau_2^2 + 1} - \frac{1}{(\omega + \omega_0)^2 \tau_2^2 + 1} \right] \tau_2. \tag{2.51}$$

In these equations τ_2 denotes the transversal relaxation time, also called the dephasing time, which describes the time period in which dephasing of the resonant tunneling system takes place. The dephasing arises due to interactions with other tunneling systems. Such interactions can take place through a change in the local strain field. A change like this can occur when tunneling systems transition or when electric interactions occur which include dipole-dipole interactions. Either way the resonant tunneling system experiences a change in energy splitting and loses coherence with the neighbouring tunneling systems. This process is called spectral diffusion and the corresponding dephasing time has been found through polarization echo experiments [Fic13].
Having covered the change in the dielectric function due to the interactions of one tunneling system through relaxation- (Subsection 2.4) and resonant processes, the total change of the dielectric function can now be calculated by taking into account the whole ensemble. To do this the change of the dielectric function is integrated over the energy splitting E, the tunneling energy Δ_0 and the angle θ between a dipole and electric field.
For the contribution of the ensemble due to relaxation processes we find

$$\frac{\delta\varepsilon'_{\mathrm{rel}}}{\varepsilon'} = \int_0^{\pi} \cos^2\theta \sin\theta d\theta \int_{\Delta_{0,\min}}^{E_{\max}} \int_{\Delta_{0,\min}}^{\mathrm{E}} dE d\Delta_0 \delta\varepsilon'_{\mathrm{rel}} P(E, \Delta_0), \tag{2.52}$$

$$\frac{\delta\varepsilon''_{\mathrm{rel}}}{\varepsilon'} = \int_0^{\pi} \cos^2\theta \sin\theta d\theta \int_{\Delta_{0,\min}}^{\mathrm{E}_{\max}} \int_{\Delta_{0,\min}}^{\mathrm{E}} dE d\Delta_0 \delta\varepsilon''_{\mathrm{rel}} P(E, \Delta_0). \tag{2.53}$$

Similarly for the contribution of the ensemble due to the resonant processes we find

$$\frac{\delta\varepsilon'_{\mathrm{res}}}{\varepsilon'} = \int_0^{\pi} \cos^2\theta \sin\theta d\theta \int_{\Delta_{0,\min}}^{\mathrm{E}_{\max}} \int_{\Delta_{0,\min}}^{\mathrm{E}} dE d\Delta_0 \delta\varepsilon'_{\mathrm{res}} P(E, \Delta_0), \tag{2.54}$$

$$\frac{\delta\varepsilon''_{\mathrm{res}}}{\varepsilon'} = \int_0^{\pi} \cos^2\theta \sin\theta d\theta \int_{\Delta_{0,\min}}^{\mathrm{E}_{\max}} \int_{\Delta_{0,\min}}^{\mathrm{E}} dE d\Delta_0 \delta\varepsilon''_{\mathrm{res}} P(E, \Delta_0). \tag{2.55}$$

With these equations the changes of the real and imaginary part were evaluated. The result of this numerical evaluation is shown in Figure 2.7. The Figure shows the influence of relaxation processes, resonant processes and the sum of both, in dependence of the temperature of the system, on the real and imaginary part.

From Figure 2.7 it is apparent that for both the real- and imaginary part, the resonant interactions dominate at low temperatures. This is because the number of phonons is very low in this temperature regime. For very low temperatures an almost temperature independent behaviour is seen since almost all tunneling systems remain in their ground state and interact resonantly with the electric field.

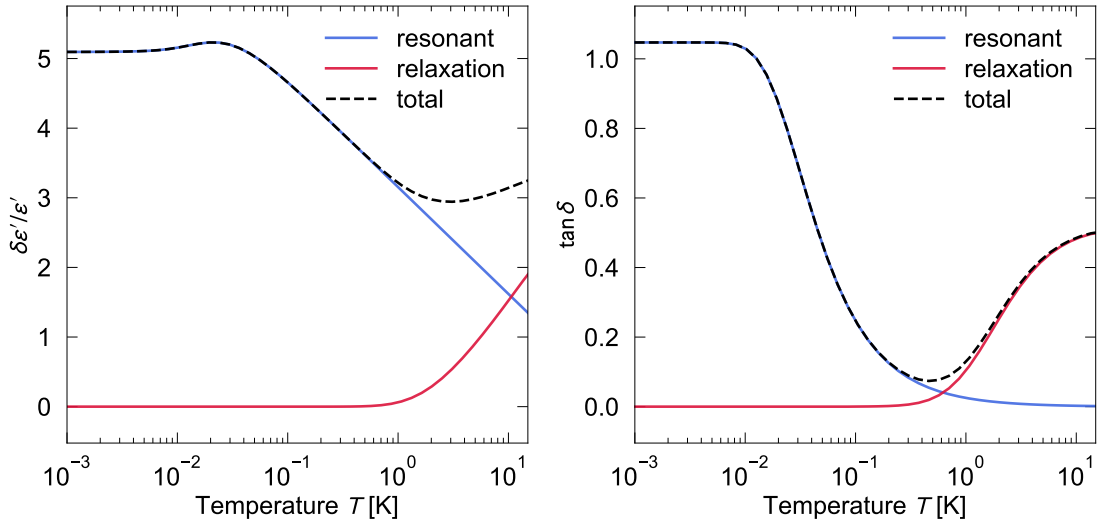

Figure 2.7: Change in the dielectric function due to relaxation- and resonant processes as a function of temperature. On the left the change in the real part of the dielectric function is depicted and on the right the dielectric loss. Adapted from [Fre21].

For the real part the behaviour is seen for $T \lesssim 0.0025\,\mathrm{K}$ and for the imaginary part for a temperature of $T \lesssim 0.002\,\mathrm{K}$. The small increase in the real part at $T \approx 0.0065\,\mathrm{K}$ is because the resonant tunneling systems become thermally accessible when $k_\mathrm{B}T \approx \hbar\omega$ is fulfilled. After that the resonant contribution decreases because tunneling systems begin to get thermally excited until at high temperatures only off-resonant tunneling systems with large energy splittings can still contribute. Further, at higher temperatures ($T \approx 0.5\,\mathrm{K}$) the relaxation processes also begin contributing and dominate the change of the dielectrics real part. As a result, a minimum is reached after which the real part increases again.
The contribution to the imaginary part is also dominated by resonant tunneling systems at very low temperatures. At these low temperatures all tunneling systems in the resonance band are able to contribute since they remain in their ground state. As the temperature increases the imaginary part decreases since the tunneling systems continue to be thermally excited until almost all become saturated. At this point the relaxation processes dominate the contribution and a minimum in the total contribution is reached. After that the contribution due relaxation processes increases until reaching a plateau. The plateau is reached because a balance is

established between the relaxation and the subsequent excitation of the tunneling systems.

2.6 Landau-Zener transitions

In the previous sections the effects of a high energy probing field on tunnelling systems were discussed. In this section we will go through the impact an additional electric bias field $F_{\mathrm{b}}(t)$ has on tunneling systems. When such an electric field is applied it modifies the energy splitting according to

$$E_{\mathrm{mod}}(t) = \sqrt{\Delta_0^2 + (\Delta + \delta\Delta(t))^2}. \tag{2.56}$$

Additionally, to the electric probe field that causes the change in the asymmetry energy $\delta\Delta$, an oscillating electric field will be applied in form of a triangle signal. This field can be modified either through the variation of the bias voltage or the frequency of the signal. This will result in a further modification of the energy splitting E which means that other tunneling systems will be in resonance with the electric probe field. Since the parameter distribution of the tunneling systems is flat it should not make any difference in the change of the real dielectric function. However, when the additional electric field is constantly changed a dynamic shift will occur which forces the tunneling systems successively through the resonance band. As a result, the tunneling systems will be consecutively excited by the electric field and thus the dielectric loss will increase. Hence, the next step is to find the dielectric loss based on the calculations of [Kha13, Bur13].
If only the tunneling systems are considered to contribute to the resonant loss that are in resonance with the high frequency probe field for which $E \approx \hbar\omega$ holds, then, a first order Taylor-approximation can be used to calculate the modification of the energy splitting around the resonance band, where only tunneling systems with $\delta\Delta \to 0$ are relevant, as

$$E_{\mathrm{mod}}(t) \approx \hbar\omega + \sqrt{1 - \left(\frac{\Delta_0}{\hbar\omega}\right)^2}\,\delta\Delta(t). \tag{2.57}$$

Next, the change of the energy splitting with time is examined

$$\frac{dE_{\mathrm{mod}}(t)}{dt} = \hbar\nu = \sqrt{1 - \left(\frac{\Delta_0}{\hbar\omega}\right)^2}\,2p\dot{F}_{\mathrm{b}}\cos\theta = \hbar\nu_0\sqrt{1 - \left(\frac{\Delta_0}{\hbar\omega}\right)^2} \tag{2.58}$$

in which we defined $\nu_0 := 2p\dot{F}_{\mathrm{b}}/\hbar$. Now the energy splitting can be rewritten as

$$E_{mod}(t) = \hbar\omega(t - t_0) \tag{2.59}$$

with t_0 being the time at which the tunneling system is in exact resonance with the field.
In a next step, we want to deduce the Landau-Zener equations by firstly solving the time dependent Schrödinger equation. In order to do this we begin to describe a system on which we impose an oscillating electric field $\boldsymbol{F}_{\mathrm{ac}}(t) = \boldsymbol{F}_{\mathrm{ac}} \cos(\omega t)$ with the wave function

$$\langle \Psi | = \begin{pmatrix} c_1(t) \\ c_2(t) \end{pmatrix} \tag{2.60}$$

which describes a superposition of the ground state $\left(\begin{smallmatrix} 0 \\ 1 \end{smallmatrix}\right)$ and the excited state $\left(\begin{smallmatrix} 1 \\ 0 \end{smallmatrix}\right)$. The time evolution can be described through the Schrödinger equation with the Hamilton operator

$$H = \frac{1}{2} \begin{pmatrix} E & 0 \\ 0 & -E \end{pmatrix} + \frac{1}{E} \begin{pmatrix} \Delta & \Delta_0 \\ \Delta_0 & -\Delta \end{pmatrix} p_0 F_{\mathrm{ac}} \cos(\omega t) \tag{2.61}$$

by neglecting relaxation processes during the resonance crossing and assuming that the change of the energy splitting in accordance to the probe field remains small, such that $E_{mod}/2 \ll \Delta/E\boldsymbol{p}\boldsymbol{F}_{\mathrm{ac}}$. As a result, the coupled equations

$$i\hbar \dot{c_1}(t) = \frac{E_{\mathrm{mod}}}{2} c_1(t) + \hbar \Omega_{\mathrm{R}} \cos(\omega t) c_2(t), \tag{2.62}$$

$$i\hbar \dot{c_2}(t) = \frac{E_{\mathrm{mod}}}{2} c_2(t) + \hbar \Omega_{\mathrm{R}} \cos(\omega t) c_1(t) \tag{2.63}$$

are found which are then transformed into the rotating frame by

$$\begin{pmatrix} a_1(t) \\ a_2(t) \end{pmatrix} = \begin{pmatrix} c_1(t) e^{i\omega t/2} \\ c_2(t) e^{-i\omega t/2} \end{pmatrix} \tag{2.64}$$

in order to find the stationary solutions

$$\dot{a_1}(t) = -\frac{i\nu}{2}(t - t_0) a_1(t) - \frac{i\Omega_{\mathrm{R}}}{2} a_2(t), \tag{2.65}$$

$$\dot{a_2}(t) = -\frac{i\nu}{2}(t - t_0) a_2(t) - \frac{i\Omega_{\mathrm{R}}}{2} a_1(t) \tag{2.66}$$

which can be identified as the equations of the Landau-Zener problem [Zen32]. In these equations the Rabi-frequency

$$\Omega_{\mathrm{R}} = \Omega_{\mathrm{R},0} \cos\theta \frac{\Delta_0}{E} \quad \text{with} \quad \Omega_{\mathrm{R},0} = \frac{pF_{\mathrm{ac}}}{\hbar} \tag{2.67}$$

was used which represents the frequency at which the oscillation between the ground- and excited state takes place when an external electric field $F_{\mathrm{ac}}(t)$ is applied.

Next, we want to look at two different extremes. First, it is assumed that the change in the energy splitting of the tunneling system is performed slowly meaning $\nu_0 \ll \Omega_{\mathrm{R},0}^2$. If this is the case then the transition to the excited state occurs under the absorption of a photon from the electric probe field. On the other hand, if the modification in the energy splitting happens fast, meaning $\nu_0 \gg \Omega_{\mathrm{R},0}^2$, there will be no excitation because the coupling between the two energy levels is too weak. This is called a Landau-Zener transition. Thus, the probability of a transition in which an excitation occurs is

$$P_{\mathrm{g}\to\mathrm{e}} = 1 - e^{-\gamma} \quad \text{with} \quad \gamma = \frac{\pi\Omega_{\mathrm{R}}}{2\nu}. \tag{2.68}$$

Now we will look at the total dissipated energy associated with an external electric field modulated by an additional bias field. In order to calculate the total loss, we integrate over the dielectric volume and over the number of tunneling systems N that are in resonance with the external field during the time interval dt

$$d\mathcal{E} = \int dV \int dN \hbar\omega P_{\mathrm{g}\to\mathrm{e}}. \tag{2.69}$$

Further, we integrate over the distribution function

$$d\mathcal{E} = \hbar\omega P_0 V \int_0^1 d\cos\theta \int_0^{\hbar\omega} d\Delta_0 \int_{\hbar\omega-\hbar_n u dt}^{\hbar\omega+\hbar\nu dt} dE \frac{PE}{\Delta_0\sqrt{E^2-\Delta_0^2}}. \tag{2.70}$$

Lastly, it is assumed that the change in energy $\hbar\nu dt$ is small and substitute $x = \Delta_0/\hbar\omega$. We find according to [Fre21]

$$\frac{d\mathcal{E}}{dt} = \pi\omega F_{\mathrm{ac}}^2 P_0 p^2 V \int_0^1 d\cos\theta \cos^2\theta \int_0^1 \frac{P_{\mathrm{g}\to\mathrm{e}}}{\gamma} \frac{x dx}{\sqrt{1-x^2}} \tag{2.71}$$

with which the dielectric loss can be written as

$$\tan\delta = \frac{P_{\mathrm{L}}}{\omega W_0} = \frac{d\mathcal{E}}{dt}\left(\omega V \varepsilon_0 \varepsilon F_{\mathrm{ac}}^2\right)^{-1} \tag{2.72}$$

where the dissipated energy is denoted as P_{L} and the stored energy as W_0. Using equation (2.71) and assuming a very fast bias sweep $\nu_0 \gg \Omega_{\mathrm{R},0}^2$ for which the approximation $e^{-\gamma} \approx 1 - \gamma$ can be made, we find

$$\tan\delta = \tan\delta_0 = \frac{\pi P_0 p^2}{3\varepsilon_0 \varepsilon_{\mathrm{r}}} \tag{2.73}$$

in which $\tan\delta_0$ denotes the saturated loss.

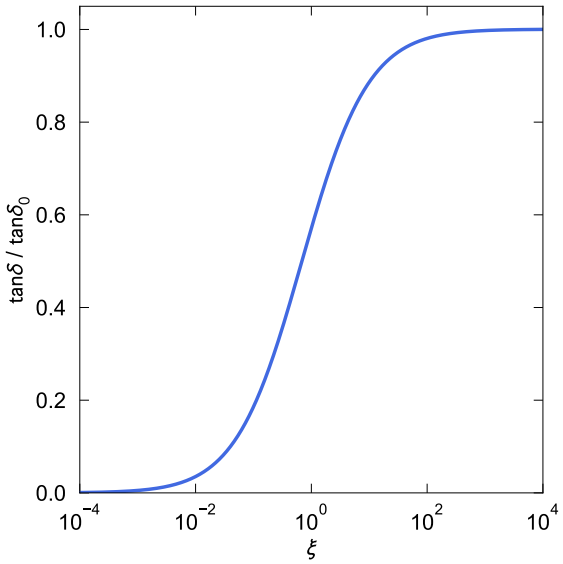

Figure 2.8: Numerical integration of the dielectric loss (2.75) in dependence of the dimensionless bias rate ξ [Kö19].

More generally, for other probe fields equation (2.72) has to be solved numerically as it was done in Figure 2.8 for which the dimensionless bias rate is defined as

$$\xi = \frac{2\nu_0}{\pi\Omega_{\mathrm{R},0}^2} = \frac{2\nu_0\hbar^2}{\pi p^2 F_{\mathrm{ac}}^2} \tag{2.74}$$

which leads to the expression

$$\tan\delta = \frac{\pi P_0 p^2}{\varepsilon_0\varepsilon_{\mathrm{r}}}\xi \int_0^1 d\cos\theta\cos\theta \int_0^1 \left(1 - \exp\left(-\frac{\cos\theta}{\xi}\frac{x^2}{\sqrt{1-x^2}}\right)\right)\frac{dx}{x}. \tag{2.75}$$

It has to be taken into account that for the calculation it was assumed that no relaxation processes occur during the resonance crossing. This assumption can be used for larger bias rates but for low ones the probability of the occurrence of relaxation processes is higher. With that in mind we can describe the behaviour of the loss for different bias rates. The loss increases for increasing bias rates and reaches a plateau at $\tan\delta_0$. This is because as the bias rate increases more tunneling systems cross the resonance band which can be potentially excited by a resonant interaction with the electric field. However, as mentioned before, the probability for a resonant interaction decreases for fast bias-sweeps. These two processes counteract each other resulting in the visible plateau.

3. Experimental Methods

This section aims to introduce the experimental setup and explain how the experimental results were obtained. To effectively measure the influence of external stimuli on the sample it is best for the tunneling systems to be in their ground state. To this end the dilution refrigerator, that is used to ensure the low temperature environment, is introduced in section 3.1. The composition of the glass sample used is explained in Section 3.2. Section 3.3 describes how the data is extracted and evaluated from the measurements. The external stimuli are provided by the electronics depicted in section 3.4 that are connected to the newly realised resonator introduced in 3.5.

3.1 Dilution refrigerators

For the experiments very low temperatures need to be achieved to ensure that most tunneling systems are in their ground state in order to effectively measure their interaction with the applied electric field. This can be illustrated by calculating the population difference for the applied frequency of $\nu = 1\,\mathrm{GHz}$ at different temperatures

$$\Delta n = \tanh\left(\frac{h\nu}{2k_\mathrm{B}T}\right) = 0.24 \quad \text{with} \quad T = 100\,\mathrm{mK}, \tag{3.1}$$

$$\Delta n = \tanh\left(\frac{h\nu}{2k_\mathrm{B}T}\right) = 0.98 \quad \text{with} \quad T = 10\,\mathrm{mK}. \tag{3.2}$$

Evidently, temperatures in the range of $T = 10\,\mathrm{mK}$ are needed. To this end, a dilution refrigerator as shown in Figure 3.1 is used. In the following a short description of the principals of dilution refrigerators will follow, a more detailed depiction can be found in [Ens05, Pob07].
A dilution refrigerator is based on the interaction between a ^{3}He/^{4}He mixture. Since the mass of a ^{4}He atom is greater than that of a ^{3}He atom it has a lower zero-point energy which makes it more favorable for ^{3}He to bind with ^{4}He rather then with with atoms of its kind. However, at some point the mixture will divide into a lighter ^{3}He-rich and into a heavier ^{3}He-poor phase. This is based in the nature of ^{3}He since it acts according to Fermi-statistics, resulting in a higher kinetic energy with increasing number density. This leads to a reduced effective binding energy. Meaning that if the concentration of ^{3}He diluted in ^{4}He gets too large, two phases are energetically more favorable. For temperatures below approximately 800 mK superfluid ^{4}He acts as a quasivacuum for ^{3}He.

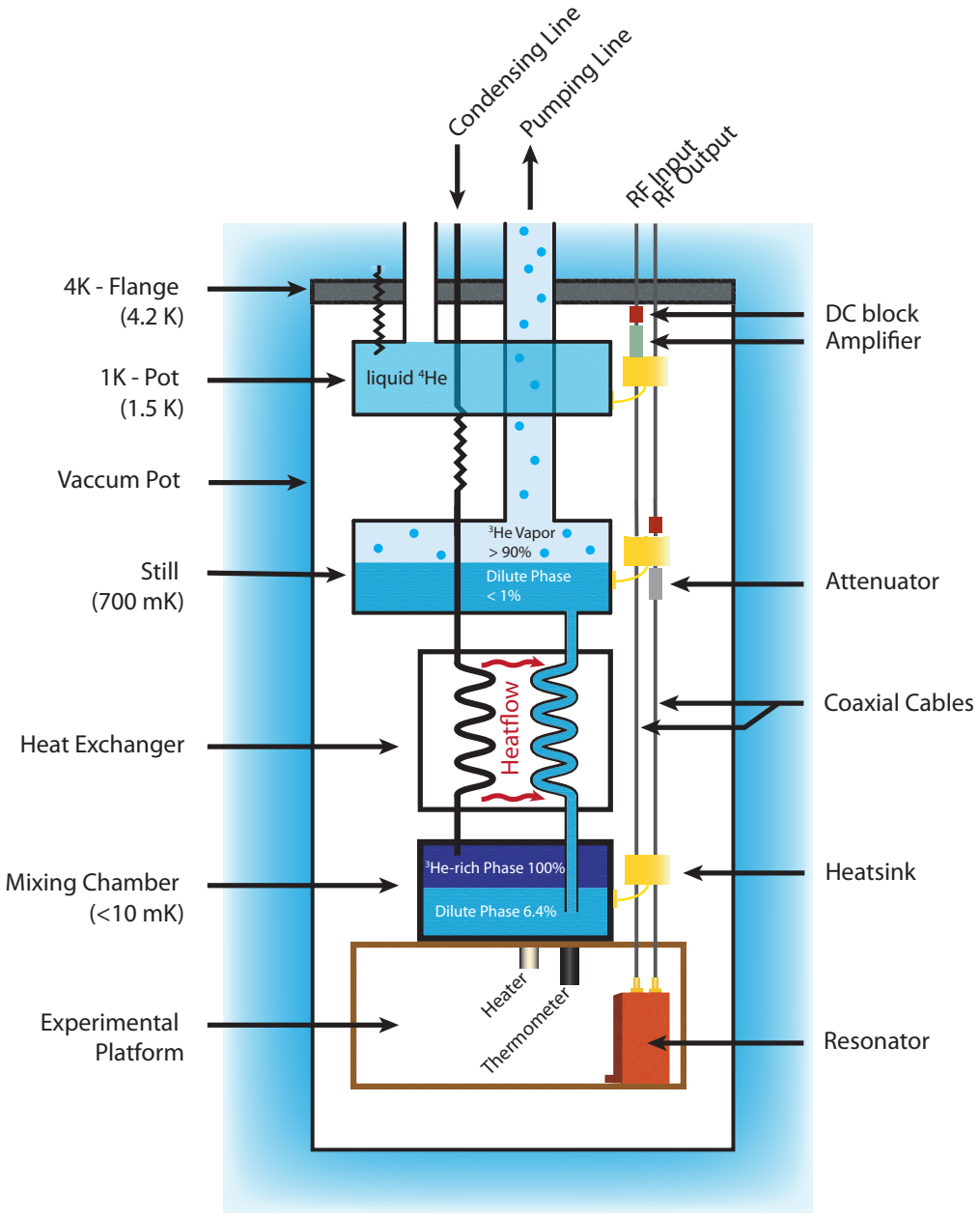

Figure 3.1: Schematic drawing of the ^{3}He/^{4}He dilution cryostat. The vacuum pot contains the dilution unit and the experiment is placed on the experimental platform. The drawing also includes part of the electronic setup that is contained within the cryostat and will be further discussed in Section 3.4. Adapted from [Pob07, Fre21].

In case of dilution refrigerators where the ^{3}He concentration is continuously reduced in the diluted phase, the explained property of ^{3}He/^{4}He mixtures leads to a continuous transition of ^{3}He from the ^{3}He rich phase to diluted phase. During this transition energy is taken in from the environment. This results in a temperature decrease with a cooling power of $\dot{Q} = 84\dot{n}_3T^2$ [Pob07] where $\dot{n}_3$ is the number of ^{3}He

atoms transitioning per unit time.
Three of the most fundamental parts of the cryostat include the mixing chamber, the still and the 1 K-pot. These components are all contained within a vacuum chamber that is submerged into a ^{4}He bath. The mixing chamber contains the diluted- and the ^{3}He-rich phase. Further, the still, that is maintained at a temperature of 0.7 K, is connected to the diluted phase and since ^{3}He has a lower boiling temperature than ^{4}He, ^{3}He is mostly evaporating inside the still through which the ^{3}He enters the pumping system. Through this process the ^{3}He concentration decreases and a concentration gradient between the still and the mixing chamber evolves that leads to an osmotic pressure. Thereby, a flow of ^{3}He from the mixing chamber to the still is set in motion which drives the phase transitions occurring in the mixing chamber. Since a continuous cycle has to be achieved for effective cooling to take place the ^{3}He is cleaned through a nitrogen- and a helium trap, enters the vacuum chamber in a capillary and is then pre-cooled in the 1 K pot. With the help of a flow impedance the pressure is maintained and ^{3}He condenses before reaching the still. In a next step, it encounters a heat exchanger and finally reaches the ^{3}He-rich phase in the mixing chamber. By using this process the temperature range needed for the experiments conducted in this thesis can be reached.
The temperature of the cryostat is measured by a resistor thermometer for which the resistance is read out through an AC resistance bridge[3] which measures the resistance through small excitation voltages to avoid parasitic heating. In addition, the temperature above a certain base temperature can be regulated by an attached heater.
To mount the experiment an experimental platform is needed. It consists of copper[4] and is therefore thermally well attached to the mixing chamber. The response of the resonator is then read out by coaxial cables that connect the resonator to the readout electronics. To reduce the heat loads from the cables heat sinks are used that are applied at different temperature steps of the cryostat.

3.2 Sample

The sample used in the experiments is the borosilicate glass N-BK7 from Schott AG[5]. The chemical composition was determined by atomic emission spectroscopy by the Fraunhofer Institute for Silicate Research and can be viewed in Table 3.1. Among the applications of this glass it has already been used for many dielectric measurements over a wide frequency range [vS75, Ant79, Woh01, Kö19, Fre21]. As a result, it is

[3] AVS-47, RV-Elektroniikka Oy Picowatt, Veromiehentie 14, FI-01510 Vantaa, Finland
[4] Tempered oxygen-free copper to avoid impurities and ensure a good thermal conductivity and thermalization of the experiments.
[5] Schott AG, Hattenbergstr. 10, 55122 Mainz, Deutschland.

SiO_2	B_2O_3	Al_2O_3	Na_2O	K_2O	BaO
74.8%	9.6%	0.03%	10.1%	4.7%	0.74%

Table 3.1: Chemical composition of the borosilicate glass N-BK7 in molar percentage [Lud03].

a good choice for the characterization of new devices since one can compare results with previous measurements. In this thesis we will focus and compare results to the results obtained in [Fre21] since similar experiments were conducted in the realm of this thesis.

3.3 Measurements

This section depicts the calculations needed to evaluate the data obtained from the experiments.

3.3.1 Characteristics of the resonator and evaluation

An external electric field is generated with the resonator which alters the state of the tunneling systems in the glass. A resonator can generally be characterized by its inductance L, capacitance C, and resistance R through which the resonance frequency

$$f_0 = \frac{1}{2\pi}\sqrt{\frac{1}{LC} - \frac{R^2}{4L^2}} \tag{3.3}$$

$$= \frac{1}{2\pi\sqrt{LC}} \qquad \text{for} \quad R = 0\ \Omega \tag{3.4}$$

can be calculated. In the second step $R = 0\ \Omega$ is declared since the resonator consists of niobium and therefore we can assume that there is no DC resistance. To analyse the response of the glass to the various external stimuli the resonance curve of the resonator will be analysed. Another parameter to describe this curve besides the resonance frequency is the internal quality factor

$$Q_\mathrm{i} = 2\pi f_0 \frac{W_\mathrm{tot}}{P_\mathrm{dis}} = R\sqrt{\frac{C}{L}} \tag{3.5}$$

which is dependent on the dissipation power $P_\mathrm{dis} = U_0^2/(2R)$ and the maximum electric energy that can be stored in the resonator $W_\mathrm{tot} = CU_0^2/2$ with U_0 being the maximum voltage. The internal quality factor excludes the coupling strength of the

resonator to the feedline Q_c so that the total quality factor of the resonator reads

$$\frac{1}{Q} = \frac{1}{Q_\mathrm{i}} + \frac{1}{Q_\mathrm{c}}. \tag{3.6}$$

The main contributors to the internal quality factor are the tunnelling systems but radiative losses, a finite electric conductivity or pair-breaking processes in superconductors might also be contributors. Since the capacitance is directly linked to the resonance frequency of the resonator we can use the relation

$$\frac{\Delta C}{C} = \frac{C - C^\star}{C^\star} = \left(\frac{f_0^\star}{f_0}\right)^2 - 1 \tag{3.7}$$

with $C^\star$, $f_0^\star$ being arbitrary reference points. However, because the electric field does not only penetrate the sample but also the volume around it we have to differentiate the capacitance of the sample C_s and the parasitic stray capacitance of the vacuum C_v, according to

$$C = C_\mathrm{s} + C_\mathrm{v}. \tag{3.8}$$

We assume the capacitance in the vacuum to be constant and because we are only interested in the change in the sample we use the relative change of capacitance within the sample

$$\frac{\Delta C_\mathrm{s}}{C_\mathrm{s}} = \frac{\Delta C}{C - C_\mathrm{v}} = \frac{\Delta C}{C} F \tag{3.9}$$

in which we introduce the filling factor $F = 1 - C_\mathrm{v}/C$ which describes the part of the electric field that penetrates the sample. As a result, the relative change of the dielectric function's real part is found to be

$$\frac{\delta\varepsilon'}{\varepsilon'} = \frac{\Delta C_\mathrm{s}}{C_\mathrm{s}} = \left(\left(\frac{f_0^\star}{f_0}\right)^2 - 1\right)\frac{1}{F}. \tag{3.10}$$

Next, through a comparison of the equations (2.72) and (3.5) the dielectric loss is determined to be

$$\tan\delta = \frac{1}{Q_\mathrm{i}}. \tag{3.11}$$

Taking into the account the influence of the stray capacitance C_v on the quality factor we write down

$$\frac{Q_\mathrm{i}}{Q_\mathrm{i,v}} = \sqrt{\frac{C}{C_\mathrm{v}}} \tag{3.12}$$

in which $Q_\mathrm{i,v}$ is the modified internal quality factor due to the stray capacitance. Overall, we find

$$\tan\delta = \frac{1}{Q_\mathrm{i,v}} = \frac{1}{Q_\mathrm{i}}\sqrt{1 + \frac{C_\mathrm{v}}{C_\mathrm{s}}} = \frac{1}{Q_\mathrm{i}\sqrt{F}}. \tag{3.13}$$

In order to extract the resonance frequency and the internal quality factor from the measured resonance curves a modified Lorentz curve

$$L(f) = A_1 + A_2\,(f - f_0) + \frac{A_3 + A_4\,(f - f_0)}{1 + 4Q^2\left(\dfrac{f - f_0}{f_0}\right)} \tag{3.14}$$

is used as a fit function. It takes into account the constant- and linear underground noise which is proportional to the parameters A_1 and A_2 respectively, the amplitude of the resonance curve A_3 and the asymmetry term which is proportional to A_4. These additional parameters have to be taken into account because the resonance curve changes according to the applied temperature, power, and bias field due to the interaction of the tunneling systems with the electric probe field. Information about the tunneling systems can be extracted from the resonator because the tunnelling systems extract energy from the resonator when they undergo resonant- and relaxation processes.

3.3.2 Landau-Zener transitions

By adding a continuously changing electric bias field, the asymmetry energies of the tunnelling systems continuously change and thus the tunneling systems are in a sense getting pushed through the resonance band. This results in an increasing dielectric loss. The change of the electric field at the capacitor is approximately given by

$$\dot{F}_\mathrm{b} \approx U_\mathrm{b} f_\mathrm{b} \left(2\left(\frac{d_1}{\varepsilon_{\mathrm{r},1}} + \frac{d_2}{\varepsilon_{\mathrm{r},2}}\right)\right)^{-1} \tag{3.15}$$

with U_b and f_b being the voltage and frequency applied through a continuous bias signal that in our case has the form of a triangle signal. The permittivity of air is denoted by $\varepsilon_{\mathrm{r},1} = 1$, $\varepsilon_{\mathrm{r},2} = 5.8$ is the absolute permittivity of N-BK7 [Fre16], $d_1 = 125\,\mu\mathrm{m}$ is the distance between the sample and the upper electrode and $d_2 = 200\,\mu\mathrm{m}$ is the thickness of the sample [Sta22]. Different bias field signals will be generated by either altering the applied voltage while keeping the frequency constant or by altering the frequency of the signal while keeping the voltage constant. The STM predicts that this should not make a difference in the measurements of the real- or imaginary part if either method is used to create the same values of the bias field. Additionally, at high bias rates created by high voltages heating effects have been observed [Kö19] that can be avoided by applying high frequencies to achieve high bias rates. It also has to be taken into account that because of the continuous application of the signal the tunneling systems will not have enough time to fully relax back into their ground state and for one tunneling system multiple coherent

Landau-Zener transitions might occur.

3.4 Signal pathway

In the following the components used in the electronic setup which can be viewed in Figure 3.2 will be introduced.

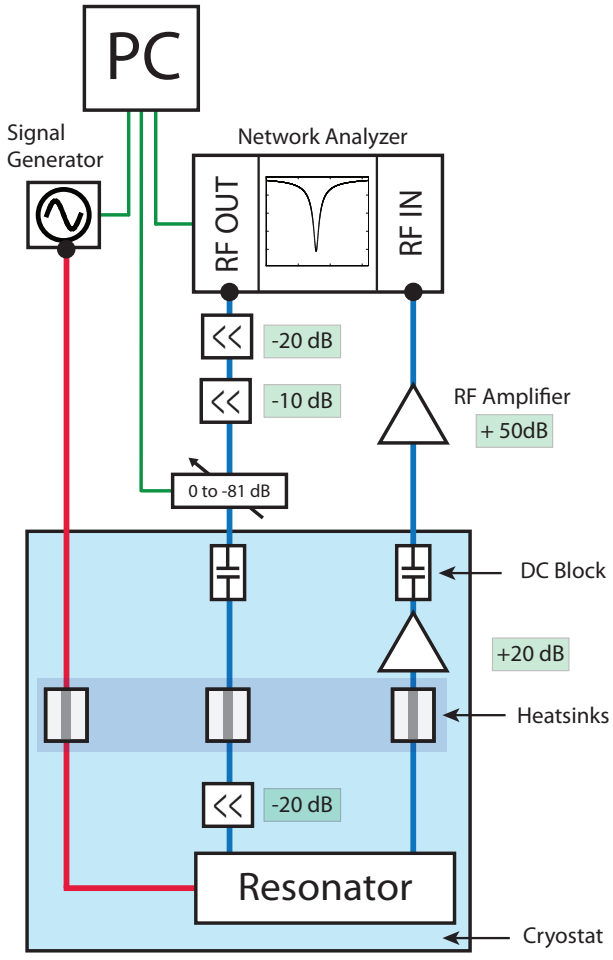

Figure 3.2: Schematic drawing of the high frequency signal pathway. The blue lines represent the electronic setup associated with the high frequency pathway, the red line is the one associated to the bias rate measurements and the green ones represent the control of the signal generator and the network analyzer by the computer via a LabView program. Adapted from [Fre21].

The signal that excites the resonator comes from a vector network analyzer[6]. It also measures the transmission in terms of amplitude and phase. Attenuators at room temperature are used to ensure that only low power signals can enter the cryostat and to reduce standing waves that emerge because of impedance differences. However, because attenuators also lead to noise another attenuator was placed inside the cryostat at lower temperatures whereby the signal to noise ratio is increased. We

[6]HP 8752A, Hewlett-Packard Company, 3000 Hanover Street, Palo Alto, CA 94304-1185 USA

use three attenuators with a fixed attenuation and one with a controllable range[7], which goes from 0 dB to −81 dB. The controllable attenuator is used to control the power that acts on the sample. To avoid heating from the coaxial cables heat sinks are used by thermally coupling the cables to the cryostat with sapphire plates at different temperature steps. Further, DC blocks are used to prevent DC- and low frequency currents from entering the resonator and the rf-amplifier[8] via the high frequency lines. The rf-amplifiers are used to enlarge the small signal that exits the resonator. The first amplifier is inside the cryostat and therefore produces less noise compared to the amplifier placed at room temperature. When the signal reaches the second amplifier it is already large enough to ensure a good signal to noise ratio.
The bias signal is created by the signal generator[9] and enters the resonator on a separate pathway.
Lastly, the network analyzer and the signal generator are connected to the computer by a GPIB[10]-port. On the computer one can control both via a LabView[11] program.

3.5 Resonator

In the following the LC-resonator used in this experiment as shown in Figure 3.3 will be described. The figure itself was constructed with the program Cadance[12]. In previous measurements [Fre21, Kö19, Lut20, Lut18] a LC-resonator with capacitors arranged in a Wheatstone-bridge setup was used. The resonator presented in this thesis is prone to less non-linearities due to its simple setup. The setup is simpler since it contains only one interdigital condensator (IDC) per resonator in contrast to the Wheatstone-bridge setup which contains four.
The chip designed for this experiment consists of five LC-resonators coupled in series that each have a different inductance and hence a differing resonance frequency. In this thesis we will only be using the resonator with the lowest resonance frequency of 1 GHz. The entire chip is microstructured onto a BK7-wafer which has a width of 200 μm. On the edge of the chip wires are placed to ensure contact between the ground plane and the actual ground. It also contributes to the thermalization of the resonator. The SMA[13] ports at the edges of the chip consist of an inner and outer cable. The inner cable is responsible for the signal pathway, whereas, the outer part

[7] Attenuator 11713A, Hewlett-Packard Company, 3000 Hanover Street, Palo Alto, CA 94304-1185 USA
[8] KUHNE electronic GmbH, Scheibenacker 3, 95180 Berg, Germany
[9] Model DS340, Standford Research Systems, 1290 Reamwood Ave, Sunnyvale, CA 94089 USA
[10] General Purpose Interface Bus
[11] LabVIEW 8.5, National Instruments Corporation, 11500 N MoPac Expwy, Austin, TX 78759-3504, USA
[12] Cadence Design Systems, 21 Oak Hill Ave, Endicott, NY 13760, US.
[13] Sub-Miniature-A.

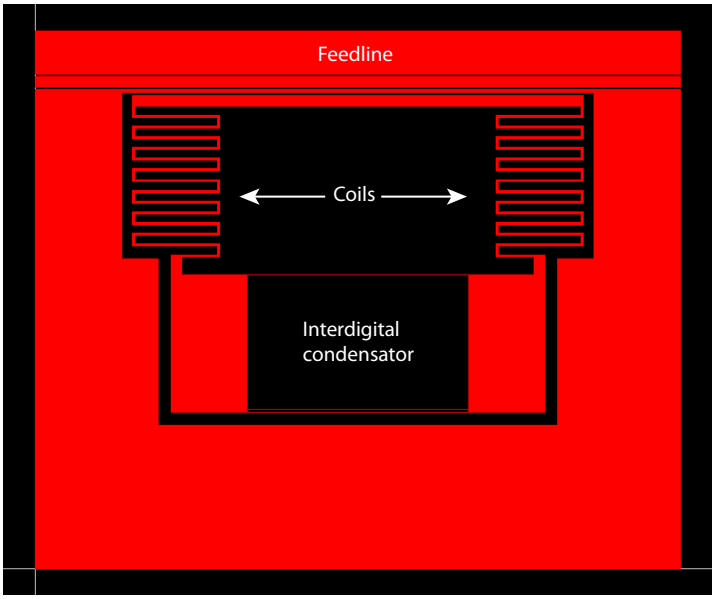

Figure 3.3: Schematic drawing made with the software Cadance of the LC-resonator used in this experiment. The resonator is on top of a layer of N-BK7 and made of niobium. The resonator is made up of 80 IDC fingers with a length of 1000 μm, a width of 6 μm and a distance of 2 μm between them [Sta22].

of the cable ensures the contact with the ground of the cryostat.
The resonator is made up of 80 IDC fingers with a length of 1000 μm, a width of 6 μm and a distance of 2 μm between them [Sta22]. The structures on top of the N-BK7 chip are made out of niobium which was sputtered and microstrutured in the institut's cleanroom. The resonator is inductively coupled to the readout electronics and separated from it by the ground plane.
The geometry of the resonator is such that the bias field and the electric probe field are perpendicular to each other and therefore do not influence the readout.
The sample case holder shown in Figure 3.4 is made of copper and is sputtered with niobium from within to shield external magnetic fields, minimize radiation losses of the resonator and avoid Eddy currents inside resistive materials.

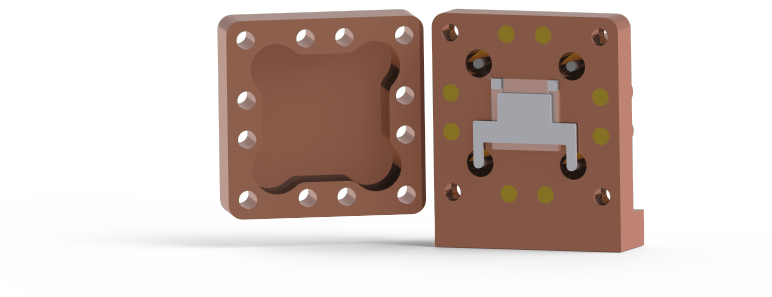

Figure 3.4: Schematic drawing of the sample case holder. The chip was inserted into it with vacuum grease which also provides thermal coupling. The bigger holes surrounding the chip are for the SMA coaxial cables which provide the bias- and probe field.

The chip is thermally coupled to the sample holder box by applying vacuum grease between them. The SMA cables come through the four big holes around the chip and are connected to the chip by aluminum wires. The bottom two SMA cables are connected to the network analyzer that creates the probe signal and the upper cables to the signal generator that provides the bias signal. The bias signal is applied by connecting the inner cable to the electrode and the outer one to the sample holder. The difference in potential between electrode and sample holder imitates a capacitor and thus provides the bias field. Aluminum wires were also used to connect the ground of the sample holder to the ground of the chip.

4. Experimental Results

In the following chapter the experimental results of this thesis will be presented. First, a characterization of the resonator is conducted in Section 4.1 to ensure a correct evaluation of the resonance curves. In addition, thermalization measurements were carried out that are depicted in Section 4.2 in order to find the time it takes for the sample to thermalize with the temperature of the cryostat. Afterwards, the individual measurements are presented and evaluated. Those measurements include dielectric equilibrium measurements, such as, the power- (Section 4.3) and temperature dependency measurements (Section 4.4) and dielectric non-equilibrium measurements that include the Landau-Zener measurements (Section 4.5). Finally, to get a better understanding of the experimental results obtained from the Landau-Zener measurements, possible heating effects occurring alongside large bias signals are analysed in Section 4.6.

4.1 Characterization of the resonator

The dielectric loss is dependent on the internal quality factor Q_i that is predominantly determined by the tunneling systems. However, the quality factor of the resonator

$$\frac{1}{Q} = \frac{1}{Q_\mathrm{i}} + \frac{1}{Q_\mathrm{c}} \tag{4.1}$$

also contains the coupling factor Q_c. To account for the coupling factor the following fit function from [Pro15]

$$S_{21}(f) = a e^{i\alpha} e^{-2\pi f \tau} \left(1 - \frac{(Q/|Q_\mathrm{c}|)e^{i\phi}}{1 + 2iQ(f/f_0 - 1)}\right) \tag{4.2}$$

will be used, which describes the transmission coefficient S_{21} of a non-ideal resonator. The function takes into account the additional scaling factor a and phase shift α, the cable delay τ and the asymmetryterm $e^{i\phi}$ due to impedance mismatches. The resonance curves that are fitted by this function are taken from the power dependency measurement at $P = -85\,\mathrm{dBm}$. Those curves have a good signal to noise ratio. Through this method the coupling factor is determined as $Q_\mathrm{c} = 11481 \pm 36$.
The results from a simulation done with the software Sonnet[14] gave a result of $Q_\mathrm{c} = 5372$ for the coupling factor. Such a deviation can be due to mistakes during the

[14]Sonnet Software, 100 Elwood Davis Road, North Syracuse, NY 13212, USA.

production of the chip. For all further evaluations the coupling factor determined by the measurements is used since it should reflect the actual chip more accurately than the simulation which treats an ideal resonator without any flaws.
Additionally, only the dielectric behaviour inside the sample is of interest. To account for that the filling factor

$$F = \frac{C_\mathrm{P}}{C_\mathrm{P} + C_\mathrm{vac}} \frac{\varepsilon_\mathrm{r} C_\mathrm{vac}}{\varepsilon_\mathrm{r} C_\mathrm{vac} + C_\mathrm{vac}} = \frac{\varepsilon_\mathrm{r}}{\varepsilon_\mathrm{r} + 1} = \frac{5.8}{6.8} \approx 0.85 \tag{4.3}$$

is used.

4.2 Thermalization measurements

The goal of the thermalization measurement is to find out how long it takes for the resonator and the sample to thermalize according to the temperature of the cryostat. For this measurement the temperature dependency of the dielectric function is used. The measurement takes place in a temperature range of 10 mK to 50 mK in steps of 5 mK at a constant power of $P = -90\,\mathrm{dBm}$. After reaching the highest temperature the temperature steps are reversed.
By plotting the temperature T, the dielectric's real part $\delta\varepsilon'/\varepsilon'$, and the dielectric loss $\tan\delta$ in dependence of time, as was done in Figure 4.1, one can see the individual temperature steps. For time $t < 8\,\mathrm{h}$ the temperature steps decrease for the real part but increase for the imaginary part. For $t > 8\,\mathrm{h}$ the opposite behaviour can be observed respectively. The real part seems to follow the temperature steps well contrasting the dielectric loss which seems less precise. Especially, at higher temperatures the dielectric loss halts its increase and even decreases slightly. This behaviour is not expected from the theoretical temperature dependency. However, the dielectric loss is large for low temperatures which means that broad resonance curves are recorded that reduce the resolution of the resonance frequency f_0. Hence, the larger imprecision of the dielectric loss compared to the real part can be expected. For low temperatures one sees an increase in the real part which coincides with the theoretical expectation as we have seen in Figure 2.7.

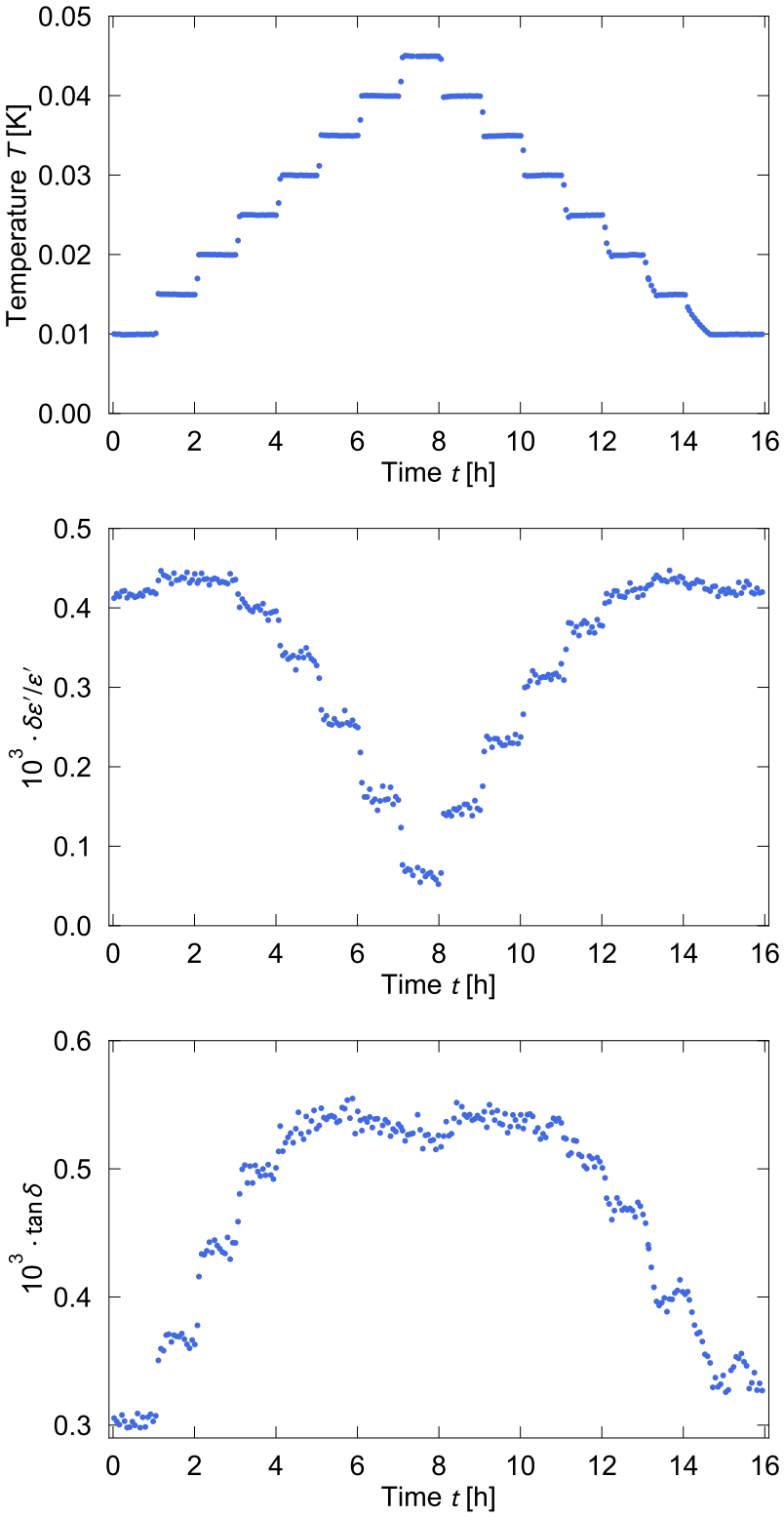

Figure 4.1: Thermalization measurements conducted on N-BK7 at a constant power $P = -90\,\mathrm{dBm}$. In the upper subfigure the applied temperature steps are depicted. The temperature steps were applied in an increasing manner that was reversed after $t = 8\,\mathrm{h}$ to test the thermalization time of the sample. The middle and bottom subfigure respectively show the real part of the permittivity and the dielectric loss.

On the first look it seems peculiar that the dielectric loss increases with increasing temperature since we have seen in the theoretical depiction of the temperature dependence (see Figure 2.7) and will see in the experimental measurements (see Figure 4.5), that it should decrease with increasing temperature. However, the measurements take place at an input power of $P = -90\,\mathrm{dBm}$ for which the loss already begins saturating as will be seen in Section 4.3. Figure 4.2 shows how the power dependency curves depend on temperature. For the numerical calculation of these curves equation (4.4) was used. The equation will be properly introduced in the next section.

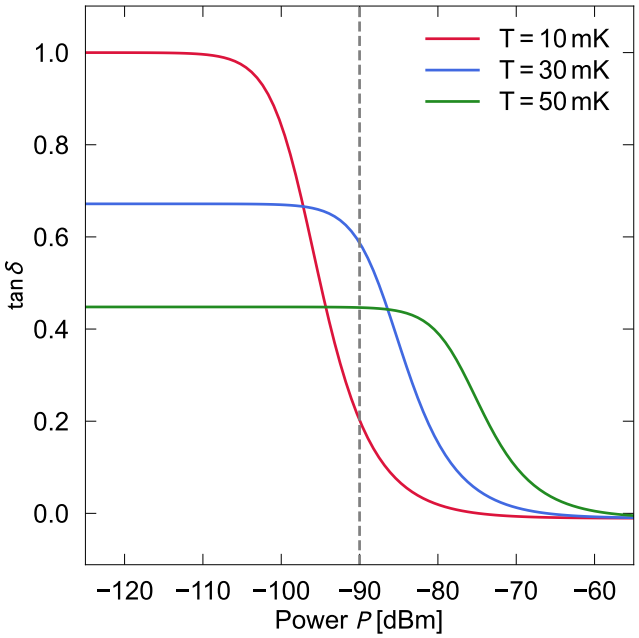

Figure 4.2: Behaviour of the power dependency curve when the temperature is increased. For the critical power the following values were used: $P_{c,1} = -97\,\mathrm{dBm}$ (red), $P_{c,2} = -87\,\mathrm{dBm}$ (blue) and $P_{c,3} = -77\,\mathrm{dBm}$ (green). Further, the parameters $A = 1.74$, $\beta = 1.73$, and $C = -1.8 \cdot 10^{-2}$ were used for the description of the power dependence curve by equation (4.4) which will be discussed in the next section.

It can be seen from Figure 4.2 that the upper plateau is at lower dielectric losses for increasing temperatures but also remains over a larger power range. This is because more tunneling systems become thermally excited at higher temperatures, thus not being able to contribute to the loss. Further, the systems that are not yet in their excited state have large energy splittings for which higher powers are needed in order to overcome them. Since the critical power P_c is the power at which the curve starts to decrease and is also dependent of the temperature, it describes the larger power range of the plateau for increasing temperatures. As a result, the increase of the dielectric loss with increasing temperature at a high power of $P = -90\,\mathrm{dBm}$ can be understood. Experimental evidence of this special case can be found in [Kö19] in which the power dependency curves were obtained at two different temperatures.
To summarize, although the dielectric loss does not follow the temperature steps as well as the real part it can still be concluded that a thermalization time of 60 min

is sufficient because of the greater imprecision of the resonance curves for large dielectric losses. The behaviours of the curves in dependency of the temperature can be explained by the introduced theory.

4.3 Power dependency

The power dependency measurements were conducted in a range of −65 dBm to −115 dBm at a constant temperature of $T = 10\,\mathrm{mK}$ by recording the resonance curves of the resonator. The different powers are adjusted by the controllable attenuator introduced in Section 3.4. Figure 4.3 shows the power dependency of the real part and dielectric loss. The individual errors of the data points seen are of statistical nature and represent the standard deviation. Further, the plot of the real part also includes the mean value of all data points and the corresponding 3σ-range.

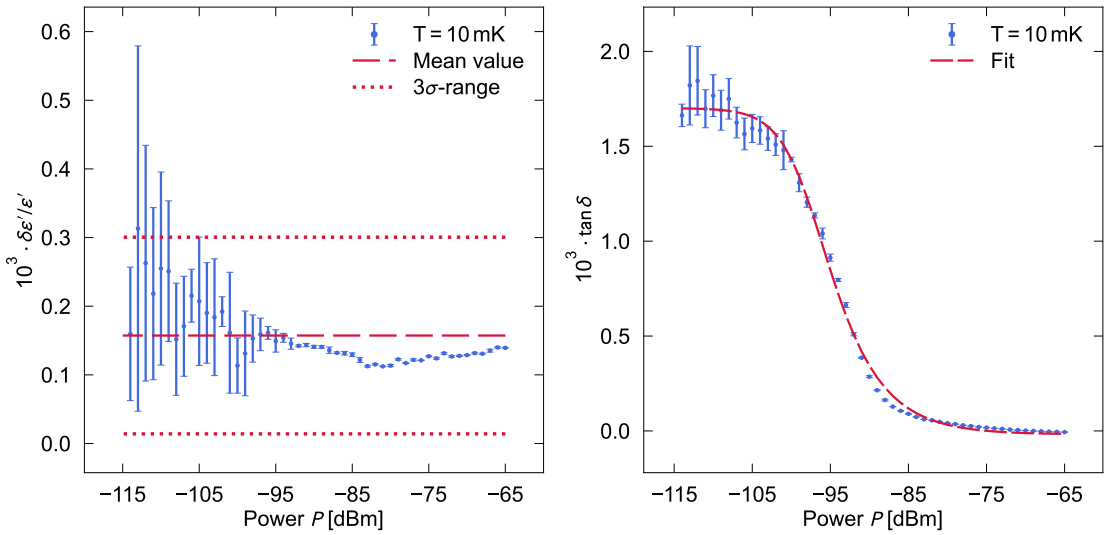

Figure 4.3: Power dependency of N-BK7. The plot of the real part contains the mean value of the measurements (dashed) and the corresponding 3σ-range (dotted).

The resonator couples with the tunnelling systems which are inside the resonance band. By altering the power, the population difference of those tunnelling systems changes. As the power increases more systems transition into the excited state. Tunnelling systems of all energy splittings contribute to the real part which leads to the observed systemic independence.
However, only tunnelling systems in the resonance band contribute to the loss resulting in the observed power dependence. For low powers only a small dependence can be seen since most tunnelling systems remain in their ground state and can con-

tribute to the loss. Since more systems become excited for higher powers, the loss decreases until finally converging towards a plateau. This behaviour can be characterized by equation (2.3).
In order to theoretically describe the behaviour of the measured dielectric loss equation (2.3) is modified to [Kö19]

$$\tan\delta = A\frac{\tanh\left(\frac{\hbar\omega}{2k_\mathrm{B}T}\right)}{\sqrt{1+\left(\frac{P}{P_\mathrm{c}}\right)^{\beta}}} + C \tag{4.4}$$

with the use of the parameters $A = \pi P_0 p^2/3\varepsilon_0\varepsilon'$, β to describe inhomogeneities of the electric field generated by the IDC, C to describe the offset that may be caused by non-resonant contributions to the loss as discussed in Section 3.3 and P_c which describes the critical power. The values for the parameters found through the fit function can be found in Table 4.1. For a homogeneous electric field the parameter is $\beta = 1$. The parameter obtained $\beta = 1.729 \pm 0.007$ deviates from a homogeneous field which might be an indication that β is not capable of fully describing the inhomogeneity of the electric field.

A	β	C $\cdot 10^{-2}$	P_c [-dBm]	χ^2	p-value
1.7474 ± 0.0006	1.729 ± 0.007	-1.810 ± 0.018	97.710 ± 0.04	0.48	0.92

Table 4.1: Parameters estimated by fitting the function (4.4) to the data of power dependency measurement.

To quantify how good the measurements and theory agree, the goodness of fit test was applied which gives a value of $\chi^2 = 0.48$ and a p-value of $p = 0.92$. Thereby, the measurements do not seem to fit the predictions well. Using a residual plot shown in Figure 4.4 one can see that the values obtained by the fit function begin deviating from the measurements for powers $P \geq -95\,\mathrm{dBm}$. This tells us that the fit function is not able to describe the saturation and the transition of the dielectric loss into the saturation. Deviations of the fit function (4.4) for power dependency measurements have also been found in [Kö19].

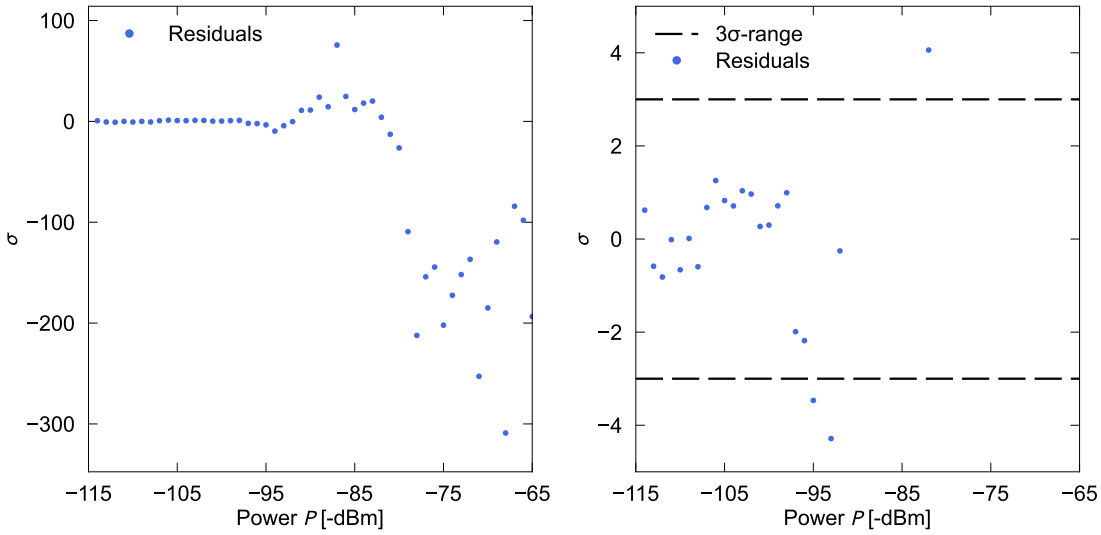

Figure 4.4: Residual plot for values obtained by the fit function (4.4) and the experimental values from the power dependency measurements. The left plot contains all residuals. In the right plot one can see in more detail which residuals are contained in the 3σ-range of the experimentally obtained dielectric loss. For powers $P \geq -95\,\mathrm{dBm}$ the residuals begin to fall outside the 3σ-range.

4.4 Temperature dependency

The dependence of the dielectric function on the temperature was measured in the range of $10^{-2}\,\mathrm{K}$ to $1\,\mathrm{K}$ at a constant power of $P = -108\,\mathrm{dBm}$. At this input power it can be ensured that the dielectric loss does not become saturated which would overshadow the thermal effects.
In Figure 4.5 the acquired data and the predictions of the STM for the temperature dependency of the dielectric function at $1\,\mathrm{GHz}$ can be viewed. The parameter $A = 1.7474$ obtained from the power dependency fit was used to scale the theory according to the experimental data.
For the real part of the dielectric function the predicted temperature independent behaviour at low temperatures cannot be seen since such low temperatures could not be reached with the dilution refrigerator. However, the small increase in the real part can be observed. This increase occurs because tunneling systems in the resonance band become thermally accessible. Afterwards, the contribution of the resonant processes decreases since less tunnelling systems are in their ground state. One can see a clear deviation of the real part from the theory for higher temperatures. Because our measurements are normalized by the maximum frequency recorded, the experimental curve reaches $\delta\varepsilon'/\varepsilon' = 0$. Thus, it cannot be accurately described by the theory.

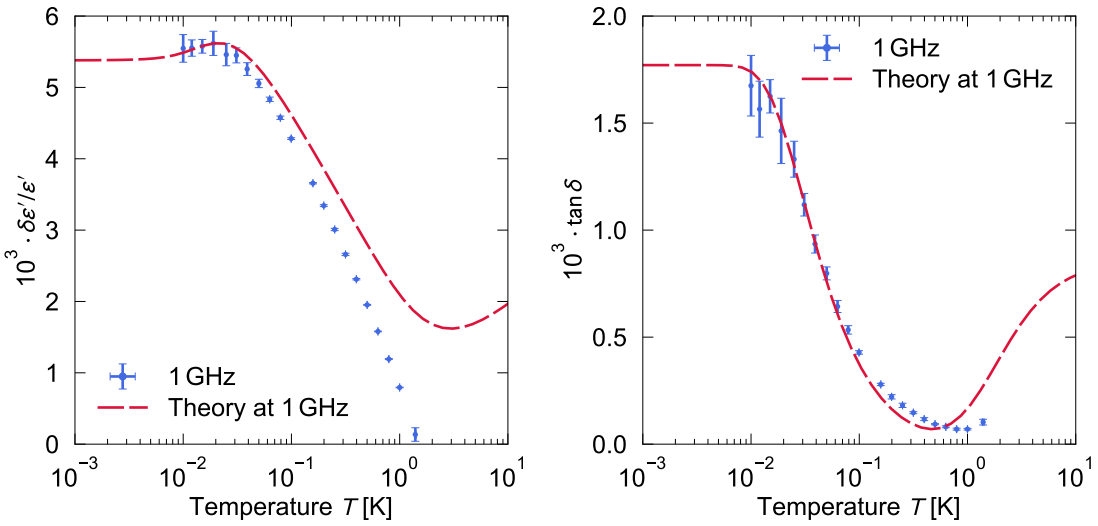

Figure 4.5: Temperature dependence of the real- and imaginary part compared to the theory discussed in Section 2.5 at 1 GHz. For the real part, the theoretical curve was shifted by the difference of the maximum between theoretical curve and experimental data. For the dielectric loss, the theoretical curve was shifted by the difference of the minimum between theoretical curve and experimental data.

For the imaginary part a flattening of the curve for low temperatures can be seen which represents the transition to the temperature independent regime. Lower temperatures could not be generated by the dilution refrigerator. Since only the tunneling systems in the resonance band contribute to the resonant processes one can observe that the resonant processes dominate for a smaller temperature range than in the real part. As the temperature increases more tunneling systems become excited and hence stop contributing to the dielectric loss. This results in the observed decrease of the curve until it reaches its minimum due to the increasing relaxation processes. All in all, the dielectric loss measured seems to fit the theory well up until $T \approx 0.1\,\mathrm{K}$. The minimum of the dielectric loss seems to have shifted to a higher temperature. This means that it takes longer for the relaxation processes to outweigh the resonant contribution.
Further, Figure 4.6 shows a comparison to the temperature measurements of the real and imaginary part conducted in [Fre21] with a Wheatstone-bridge setup at 1 GHz. The plots also include the theory used in [Fre21] to describe the experimental data. For the real part, the blue data points were shifted by the difference of the maximum values obtained in both measurements. For the imaginary part, the red data points and the theory were shifted by the difference of the minimum values obtained in both measurements. This can be done because the real part is a relative value that depends on an arbitrary reference frequency. The real- and imaginary part are both

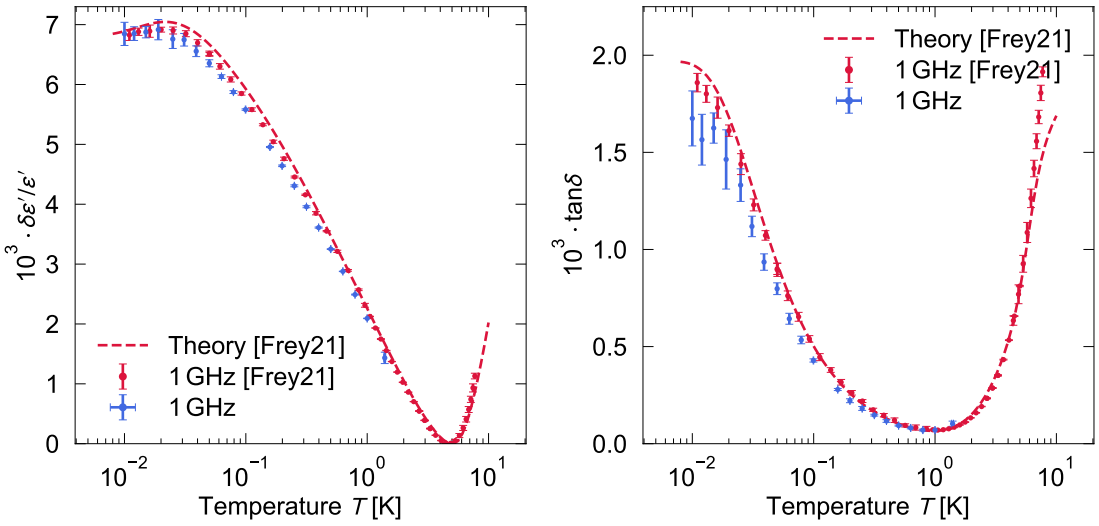

Figure 4.6: Comparison of the measured temperature dependence with the adapted data and theory of [Fre21] where a Wheatstone-bridge setup was used. For the real part, the blue curve was shifted by the difference of the maximum between the two data sets. For the dielectric loss, the red curve and the theory were shifted by the difference of the minimum between the two data sets.

dependent on the scaling factor A that differs for the two data sets.
The two measurements of the real part correspond well with each other. However, as has been observed in Figure 4.5, the theory was not able to describe the experimental data. The experimental data of [Fre21] seems well described by the theory. This is because a modified theory was used which includes the use of a different distribution function that does not assume a constant distribution of energy levels. The modified distribution function assumes a decreased number of low-energy tunneling systems due to interactions between tunneling systems. For further information the reader is referred to [Bur95, Fre16, Fre21]. The dielectric loss also shows a similar course and a slight deviation for low temperatures. Such deviations indicate that our measurement took place at a higher input power which leads to a quicker saturation of the dielectric loss. It can be also seen here that the modified theory used by [Fre21] describes the data better than the theory given by the pure STM.
Additionally, the measurements were conducted with two different dilution refrigerators which might have had different temperature calibrations. This could also lead to deviations. By shifting the red data points by $T = 10^{-3}\,\mathrm{K}$, as was done in Figure 4.7, a better agreement between the two curves can be seen. However, the red data points still reach decreased dielectric losses in comparison to the red data points. This points to the aforementioned higher input power in comparison to the

measurements of Frey.

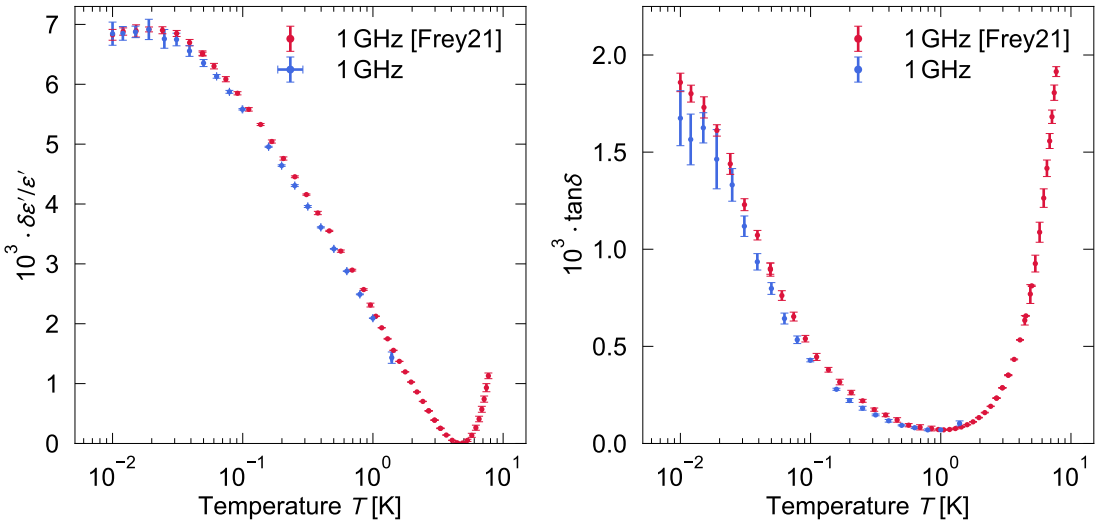

Figure 4.7: Comparison of the measured temperature dependence with the adapted data of [Fre21] where a Wheatstone-bridge setup was used. Here the red curves were shifted by the difference of the minimal temperature recorded in both data sets.

Overall, the experimental results show a good agreement with the predicted theory concerning the dielectric loss but the theory is not able to fully describe the real part. The comparison to the measurements of Frey show a good agreement.

4.5 Landau-Zener measurements

The Landau-Zener measurements were conducted for a rate of change in the range of $10^0\,\mathrm{MVs^{-1}m^{-1}}$ to $10^3\,\mathrm{MVs^{-1}m^{-1}}$, at a constant temperature of $T = 10\,\mathrm{mK}$, for three different input powers, namely $-85\,\mathrm{dBm}$, $-90\,\mathrm{dBm}$ and $-95\,\mathrm{dBm}$. The bias signal is applied in the form of a triangle signal for which either the amplitude or frequency were changed, to achieve different change rates of the bias signal.

4.5.1 Frequency dependent bias rate measurement

In Figure 4.8 the real part and the dielectric loss are depicted in dependence of the rate of change $\dot{F}_\mathrm{b}$. The bias rate was varied by changing the frequency of the signal at a constant voltage of $U_\mathrm{b} = 1.5\,\mathrm{V}$. The bias signal alters the energy splittings of the tunnelling systems and consequently new tunnelling systems enter the resonance band.

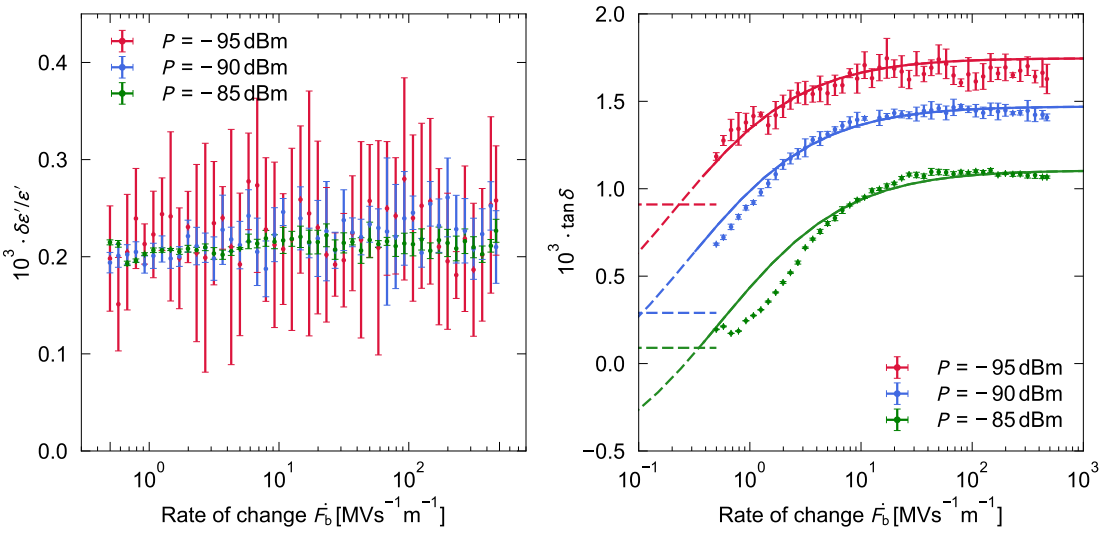

Figure 4.8: Bias rate dependence of N-BK7 at a temperature of $T = 10\,\mathrm{mK}$. The bias rate was adjusted by continuously changing the frequency of the applied triangle signal at a constant voltage $U_\mathrm{b} = 1.5\,\mathrm{V}$. The left figure shows the bias rate dependency of the real part. The right figure shows the bias rate dependency of the dielectric loss with the corresponding theory that was acquired by numerically integrating equation (2.75). The theoretical lower plateaus (dashed) were determined from the power dependency measurement. The measurements were conducted at three different input powers.

Since not only tunnelling systems in the resonance band but rather all systems contribute to the real part no dependence of the real part on the rate of change is observed.

Moving on to the bias rate dependency of the dielectric loss, the right plot of Figure 4.8 shows the measurements at different powers with the corresponding theory from equation (2.75) that was numerically integrated. The plot also shows the plateaus at low bias rates that were determined from the power dependency measurements. For all powers the lower plateau cannot be observed yet. A broader rate of change range should be used to determine the accurate position of the lower plateaus which could not be done in these measurements because the signal generator was not able to generate such low frequencies. The numerically integrated curves fit the measurements well for the lower powers. However, the measurement at the highest power shows some deviation at low bias rates. The experimental curve increases faster than the theoretically predicted one. The reason for this may lay in the way the curves were fitted by the theory. Essentially one uses the same numerically integrated curve for all measurements by shifting the curves so they fit the measurements the best. This works well at low power measurements since at low powers less tunneling systems are in the excited state. For higher powers this changes and because more tunneling systems are excited, the dielectric loss is decreased relative to the predicted curve as

seen in the plot.

4.5.2 Voltage dependent bias rate measurement

The same measurement was conducted by changing the voltage of the signal applied at a constant frequency of $f_\mathrm{b} = 10\,\mathrm{kHz}$ and can be seen in Figure 4.9.

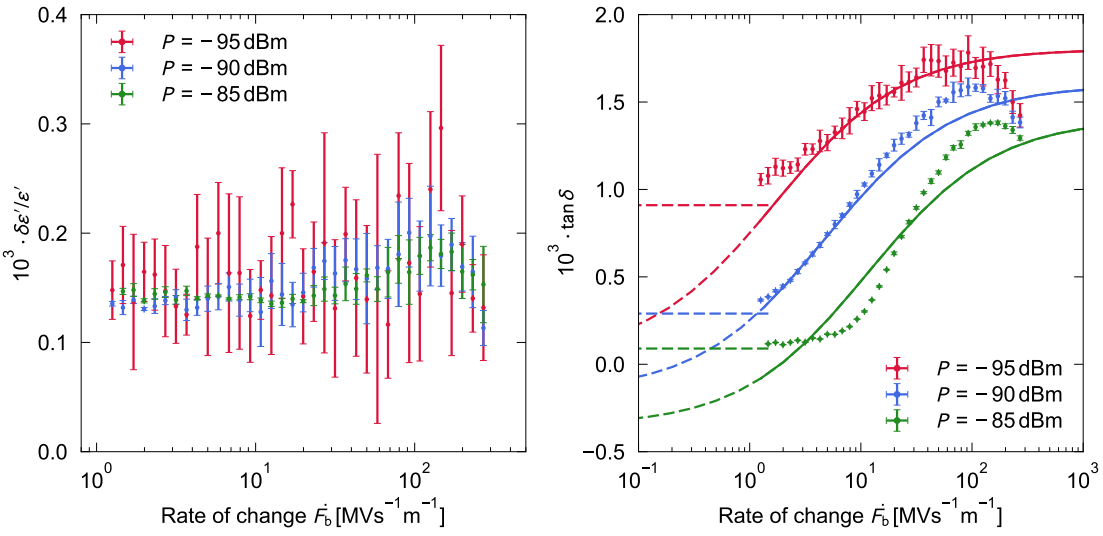

Figure 4.9: Experimentally determined bias rate dependency of N-BK7 at a temperature of $T = 10\,\mathrm{mK}$. The bias rate was adjusted by continuously changing the bias voltage of the applied triangle signal at a constant frequency $f_\mathrm{b} = 10\,\mathrm{kHz}$. The left figure shows the bias rate dependency of the real part. The right figure shows the bias rate dependency of the dielectric loss with the corresponding theory that was acquired by numerically integrating equation (2.75). The theoretical lower plateaus (dashed) were determined from the power dependency measurement. The measurements were conducted at three different input powers.

For the real part no bias rate dependency can be observed for the same reasons as before. However, in all three measurements a slight increase and subsequent decrease of the curve can be observed. Since no dependency on the bias rate can be expected other sources have to be considered such as external heating effects caused by the high voltages required to create the high rates of change. Such effects have already been observed in a previous measurement [Kö19]. A more detailed discussion to varify whether heating effects are responsible follows in the next Section 4.6.
The measurements of the dielectric loss also include the maxima that already surfaced in the measurements of the real part. This tells us that the origin of this behaviour influences all tunneling systems. Except for the unexpected maxima of the curves the theoretical prediction is able to describe the lowest power measure-

ment well. For the second measurement a deviation can be seen for higher bias rates since the maximum value of the dielectric loss has increased in comparison to the frequency dependent measurement. The last curve cannot be described well by the theoretical prediction. It has already been seen that for high bias rates the deviation occurs because the maximum value of the measurement increases in regards to the frequency dependent counterpart, thus, the theoretically predicted plateau cannot describe it accurately anymore. The deviation for low bias rates has already been seen in the frequency dependent measurement. However, it is interesting to note that the increase of the loss towards high bias rates is steeper than the increase observed in the frequency dependent measurement. This leads to a more visible lower plateau that coincides with the predicted one. The increase is also steeper for the other two measurements. As a result, it is deduced that the voltage dependent bias rate begins to affect the tunneling systems not until larger bias rates are applied but once they are affected, the dielectric loss increases very quickly. It might be that tunneling systems pass the resonance band more quickly.

4.5.3 Dimensionless bias rate

In Section 2.6 the dimensionless bias rate ξ was introduced in equation (2.74). In Figure 4.10 the bias rate measurements of the voltage- and frequency dependent bias rate are plotted respectively against ξ. The field strength for one capacitor is given by [Fre21]

$$F_{\mathrm{ac}} = \sqrt{\frac{4Q^2 P_{\mathrm{in}}}{Q_{\mathrm{c}} C d^2 \omega_0}} \tag{4.5}$$

with $d = 2\,\mu\mathrm{m}$ as the distance between the IDC fingers and the IDC capacitance $C = 3.02\,\mathrm{pF}$ was used to calculate ξ. Both parameters were obtained through a simulation in the software Sonnet [Sta22]. For the calculation of ξ the dipole moment of the sample is also needed and was approximated as $p = 1.5\,\mathrm{D}$ [Fre21]. The black curve represents the theoretical prediction through equation (2.75).
When measurements that are conducted at different powers are plotted against the dimensionless bias rate the curves are expected to collapse onto each other for high bias rates until reaching their plateaus [Mat19]. For the measurements with a voltage dependent bias rate (right) a good agreement between the theory and the experimental results can be seen. For the frequency dependent measurement (left) a collapse of the curves onto each other cannot be seen. The red curve seems to be collapsing into the blue curve. The blue curve will not necessarily merge with the green one since the curves begin separating from each other at low bias rates. As has been already discussed the voltage dependent measurement curves showed a steeper increase then

the frequency dependent curves. Since the curves collapse in on each other primarily between the lower and upper plateau this could explain the deviation.

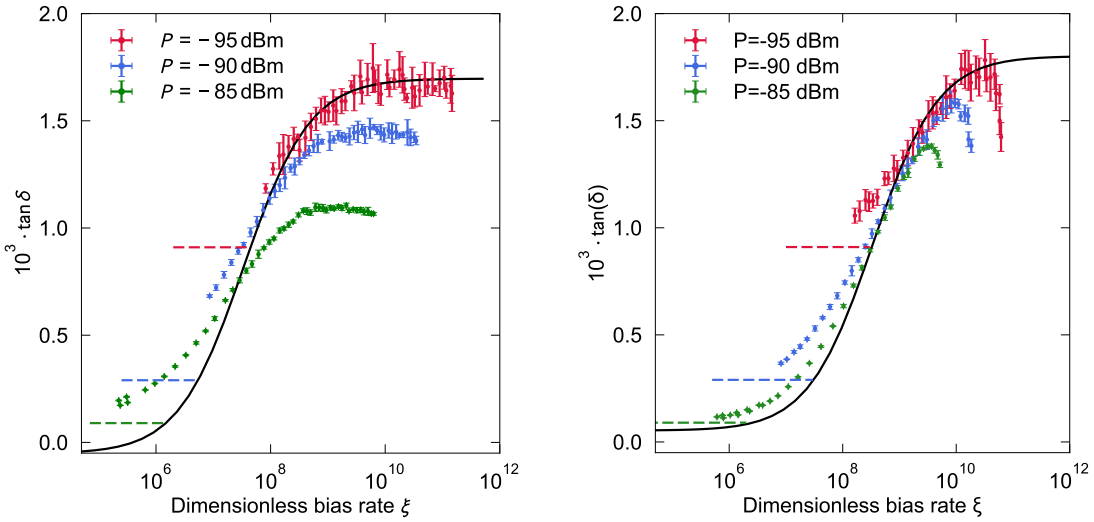

Figure 4.10: Measurements of the dielectric loss plotted against the dimensionless bias rate ξ. On the left the measurements conducted with a frequency dependent bias rate and on the right the one with a voltage dependent bias rate can be seen. The black curve represents the theoretical prediction of equation (2.75). The theoretical lower plateaus (dashed) were determined from the power dependency measurement.

To properly determine how well the theory describes the frequency dependent bias rate measurement further experiments in a broader frequency range have to be conducted. One could also see if a possible decrease of the dielectric loss would occur at higher bias rates.

4.6 Heating effects

In Figure 4.11 measurements of possible heating effects on the dielectric loss are depicted. To obtain this data a constant bias signal was applied at a power of $P = -85\,\mathrm{dBm}$ and then abruptly switched off. If no further heating takes place a constant loss of the value $\tan\delta = (0.0901 \pm 0.0024) \cdot 10^{-3}$ is expected, which was obtained from the power dependency measurement.

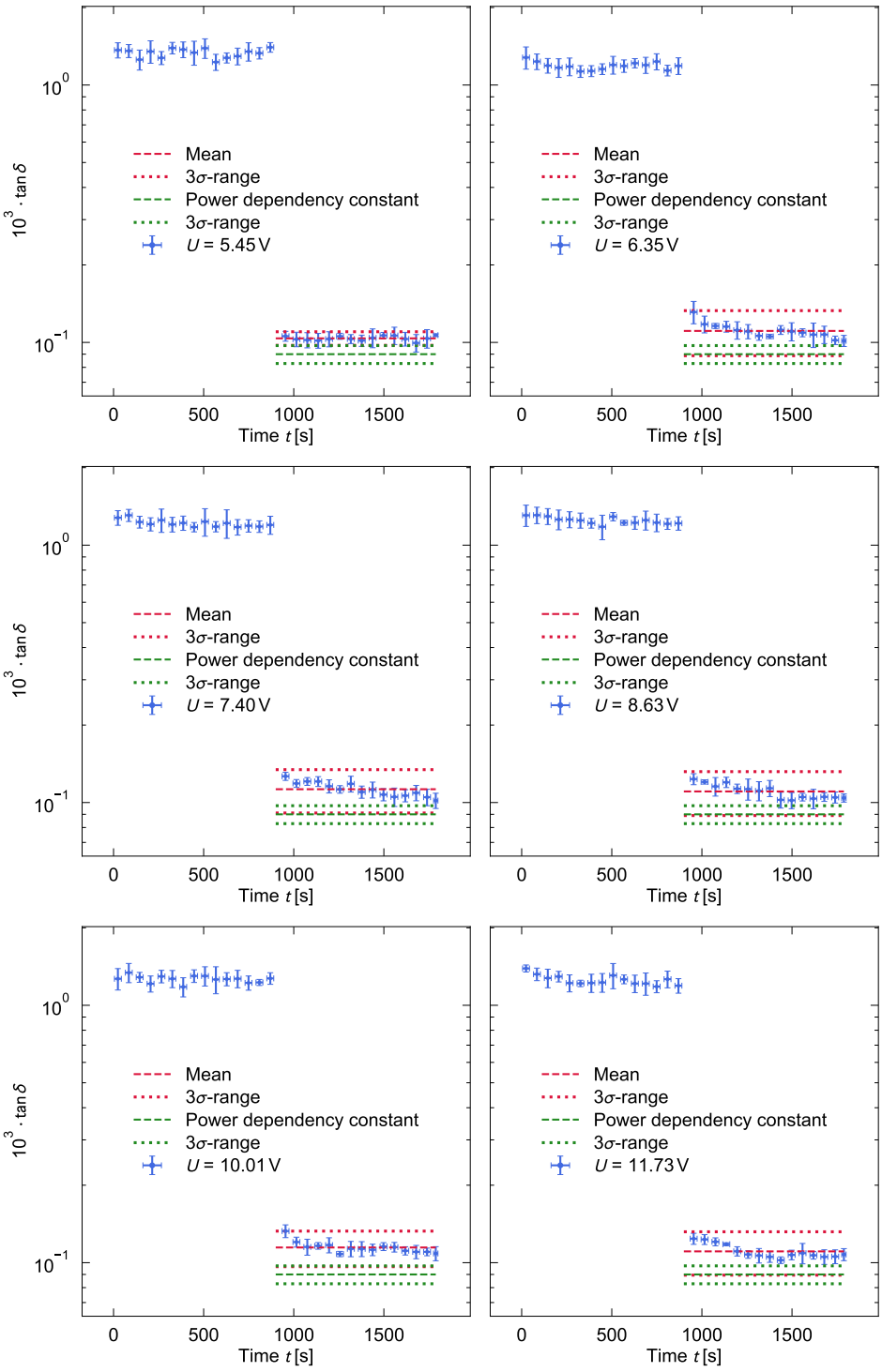

Figure 4.11: Heating effects observed by first applying a bias signal and then switching it off abruptly at a constant power $P = -85\,\mathrm{dBm}$ and constant temperature $T = 10\,\mathrm{mK}$. The plots include the corresponding mean values (red, dashed) and the 3σ-range (red, dotted). Further it contains the constant value of the dielectric loss expected at $P = -85\,\mathrm{dBm}$ (green, dashed) and it's 3σ-range (green, dotted).

For one, a slight decrease in the measured data points after switching off the signal can be seen, however, all data points remain in the 3σ-range of their mean value. Therefore, it cannot be concluded that the decrease has a statistical significance. Further, the constant loss at $P = -85\,\mathrm{dBm}$ was plotted in green with the corresponding 3σ error range. Although all data points are greater than the expected value, the 3σ-ranges of the expected and the mean of the experimental values overlap. As a result, a possible trend is acknowledged but no statistically significant heating effects can be determined that influenced the previous measurement.
As a result, other sources have to be considered. It would make sense that a quicker pass through the resonance band would lead to a steeper increase because more tunneling systems could contribute to the loss. However, this should also lead to the curves culminating in a plateau at lower bias rates. As seen in Figures 4.8 and 4.9, this is not the case. Further, there must also be an effect that causes the tunneling systems to stay longer in their ground state since the lower plateaus can be found at higher bias rates in comparison to the frequency dependent measurement.

5. Conclusion and Outlook

The goal of this thesis was to show that a novel resonator setup can be used to analyse amorphous solids as well as the Wheatstone-bridge setup which has been used in previous theses. This was done by characterizing the resonator and conducting measurements that were compared to the theory from the STM and previous measurements.
The characterization of the resonator included the determination of the coupling factor through a fit function that describes the transmission coefficient of a non-ideal resonator and accounts for the cable delay and impedance mismatches of the electronic setup. With this method the coupling factor was determined as $Q_\mathrm{c} = 11481 \pm 36$. The filling factor was calculated as $F \approx 0.85$.
In order for the experiments to be conducted successfully, thermalization measurements were made to find out how long it takes for the sample and the resonator to adapt to temperature changes in the dilution refrigerator. The measurements showed a good agreement with the theoretical expectations. Thus, it was concluded that $t = 60\,\mathrm{min}$ is a sufficient thermalization time.
Next, characterization measurements of the resonator were conducted. These included power- and temperature dependency measurements. The power dependency measurements showed that the real part does not experience any dependency of the input power. The dielectric loss was fitted by a function that reflects the expectations from the STM. The goodness of fit test was conducted and the value $\chi^2 = 0.48$ as well as the p-value $p = 0.92$ were found which indicate that the measurements do not fit the predictions of the model well. A residual plot further revealed that the fit fails for powers $P \geq -95\,\mathrm{dBm}$. Deviations of the fit function and power dependency measurements have also been seen in [Kö19]. Nevertheless, through the fit the scaling factor $A = 1.7474 \pm 0.0006$ was found which was used in the subsequent evaluation of other measurements to scale the theory accordingly. This worked quite well since the fit is able to describe the upper plateau of the measurement. Also the parameter $\beta = 1.729 \pm 0.007$ was determined and is supposed to describe the inhomogeneity of the electric probe field. A homogeneous electric field would be described by $\beta = 1$. This indicates that the parameter β is not able to fully describe the inhomogeneity of the field.
The temperature dependency measurements were compared to the predictions from the STM but also previous measurements conducted in [Fre21]. Generally, the measurements show the expected behaviour which includes a dominance of the resonant interactions at low temperatures and an increasing importance of relaxation processes for higher temperatures. However, the real part could not be fully described

by the STM. This is because the experimental data is normalized with a reference frequency which is the largest frequency recorded. The imaginary part shows a good agreement up until $T \approx 0.1\,\mathrm{K}$. The minimum of the curve seems to have shifted to higher temperatures. This indicates that it takes higher temperatures for the relaxation processes to compensate the resonant interactions.
The comparison to the measurements of [Fre21] show a good agreement, except for the imaginary part at low temperatures. This can be because a higher input power for the measurements was used and because the temperature calibration of the dilution refrigerators differs. When accounting for a possible deviation of the temperature calibration, the measurements show a good agreement but still indicate that for the measurements in this thesis a larger input power was used. Further, the theory that Frey used to describe his data is able to describe it well in contrast to the pure STM that could not fully describe the measurements in this thesis. This is because the theory used by Frey accounts for interactions between tunneling systems.
Finally, the effect of an electric bias field on the sample was measured and compared to the theoretical expectations. The frequency dependent bias signal showed a good agreement, whereas the voltage dependent signals showed some unexpected behaviour. For one, a steeper increase of the curves can be observed in comparison to the frequency dependent measurement. Further, the curves decrease after reaching their maximum value. Heating of the sample was considered as a possible explanation but disproved by measurements that targeted possible heating effects.
Both measurements were also plotted against a dimensionless bias rate ξ which should lead the curves to collapse onto each other. This behaviour can be seen for the voltage dependent measurements but only partly for the frequency dependent ones. This could be because the frequency dependent curves do not show the full course of the curve. To get a complete picture one needs to measure over a wider bias rate range which was not possible with the given signal generator.
Future experiments with the presented type of resonator will include a wider bias rate range and hopefully shed further light on the behaviour of the sample under influence of electric bias fields. Additionally, pump tones are being used to excite off-resonant tunneling systems, push them through the resonance band with an electric bias field, as was done in this thesis, in order to observe possible effects. Lastly, a new way to analyse amorphous solids is being tested, which involves adding the possibility of changing the asymmetry energy by adding a mechanic distortion field. It will be seen if both fields have similar effects on the energy levels of the tunneling systems.
In conclusion, the experiments showed that the novel resonator design can be used for the experimentation on amorphous solids and has the potential to be used for new kinds of experiments.

Bibliography

[And72] P. W. Anderson, B. I. Halperin, and C. M. Varma, Anomalous low-temperature thermal properties of glasses and spin glasses, *Phil. Mag.*, **25**, 1, 1972.

[Ant79] P. J. Anthony and A. C. Anderson, Frequency and temperature dependence of dielectric and ultrasonic dispersion in amorphous materials at low temperatures, *Phys. Rev. B*, **20**, 763–767, 1979.

[Bur95] A. L. Burin, Dipole gap effects in low energy excitation spectrum of amorphous solids. theory for dielectric relaxation, *J. Low Temp. Phys.*, **100**(3), 309–337, 1995.

[Bur13] Alexander L Burin, Moe S Khalil, and Kevin D Osborn, Universal dielectric loss in glass from simultaneous bias and microwave fields, *Physical Review Letters*, **110**(15), 157002, 2013.

[Dou80] P. Doussineau, C. Frénois, R. G. Leisure, A. Levelut, and J.-Y. Prieur, Amorphous-like acoustical properties of Na doped $\beta - Al_2O_3$, *J. Phys France*, **41**, 1193, 1980.

[Ell84] S. R. Elliott, *Physics of Amorphous Materials*, Longman, London, 1984.

[Ens05] C. Enss and S. Hunklinger, *Low-Temperature Physics*, Springer, Heidelberg, 2005.

[Fic13] G. Fickenscher, *Phasenkohärenz und Energierelaxation von Tunnelsystemen in Gläsern*, Dissertation, Heidelberg University, 2013.

[Fre16] B. Frey, Entwicklung mikrostrukturierter supraleitender resonatoren zur breitbandigen untersuchung dielektrischer eigenschaften zwischen 37 mhz und 1 ghz bei tiefen temperaturen, 2016.

[Fre21] Benedikt Frey, *Landau-Zener spectroscopy of bulk glasses*, Dissertation, 2021.

[Hun72] S. Hunklinger, W. Arnold, St. Stein, R. Nava, and K. Dransfeld, Saturation of the ultrasonic absorption in vitreous silica at low temperatures, *Phys. Lett. A*, **42**(3), 253 – 255, 1972.

[Hun74] S. Hunklinger, Ultrasonics in amorphous materials, *Proc. Ultrasonic Symp. (IEEE)*, 1974.

[Hun76] S. Hunklinger and W. Arnold, 3 - Ultrasonic properties of glasses at low temperatures, Volumen 12 in *Phys. Acoust.*, 155 – 215, Academic Press, 1976.

[Hun18] Siegfried Hunklinger, *Festkörperphysik*, De Gruyter Studium, De Gruyter, Berlin ; Boston, 5. auflage edition, 2018.

[Jä72] J. Jäckle, On the ultrasonic attenuation in glasses at low temperatures, *Z. Phys. A*, **257**(3), 212, 1972.

[Kha13] M. S. Khalil, *A study of two-level system defects in dielectric films using superconducting resonantors*, Dissertation, University of Maryland, 2013.

[Kha14] M. S. Khalil, S. Gladchenko, M. J. A. Stoutimore, F. C. Wellstood, A. L. Burin, and K. D. Osborn, Landau-Zener population control and dipole measurement of a two-level-system bath, *Phys. Rev. B*, **90**, 100201, 2014.

[Kö19] D. Körner, Nichtgleichgewichtsdynamik von Tunnelsystemen im Bor-Kronglas N-BK7 bei 1 GHz und tiefen Temperaturen, 2019.

[Luc16] A. Luck, *Nuclear spin dominated relaxation of atomic tunneling systems in glasses*, Dissertation, Heidelberg University, 2016.

[Lud03] S. Ludwig, P. Nagel, S. Hunklinger, and C. Enss, Magnetic field dependent coherent polarization echoes in glasses, *J. Low Temp. Phys.*, **131**, 89–111, 2003.

[Lut18] S. Lutter, Dielektrische Messungen der Nichtgleichgewichtsdynamik wechselwirkender Tunnelsysteme in Gläsern bei tiefen Temperaturen, 2018.

[Lut20] M. Lutz, Dielektrische Eigenschaften von N-BK7 bei 1 GHz unter Einfluss einer großen statischen Polarisation bei sehr tiefen Temperaturen, 2020.

[Mat19] S. Matityahu, H. Schmidt, A. Bilmes, A. Shnirman, G. Weiss, A. V. Ustinov, M. Schechter, and J. Lisenfeld, Dynamical decoupling of quantum two-level systems by coherent multiple landau–zener transitions, *npj Quantum Inf.*, **5**, 114, 2019.

[Mü21] Lukas Münch, Simulations of the non-linear behavior of two-level atomic tunneling systems, 2021.

[Nal04] P. Nalbach, D. Osheroff, and S. Ludwig, Non-equilibrium dynamics of interacting tunneling states in glasses, *J. Low Temp. Phys.*, **137**(3-4), 395–452, 2004.

[Phi72] W. A. Phillips, Tunneling states in amorphous solids, *J. Low Temp. Phys.*, **7**, 351–360, 1972.

[Phi81] W. A. Phillips (Ed.), *Amorphous solids*, Volumen 24 in *Topics in current physics*, Springer, Heidelberg, 1981.

[Pob07] F. Pobell, *Matter and methods at low temperatures*, Springer, Berlin ; Heidelberg, 3. edition, 2007.

[Pro15] S. Probst, F. B. Song, P. A. Bushev, A. V. Ustinov, and M. Weides, Efficient and robust analysis of complex scattering data under noise in microwave resonators, *Rev. Sci. Instrum.*, **86**(2), 024706, 2015.

[Sta22] Christian Staender, Private Communication, 2022.

[vS75] M. von Schickfus, S. Hunklinger, and L. Piché, Anomalous dielectric dispersion in glasses at low temperatures, *Phys. Rev. Lett.*, **35**, 876–878, 1975.

[vS77] M. von Schickfus and S. Hunklinger, Saturation of the dielectric absorption of vitreous silica at low temperatures, *Phys. Lett.*, **64 A**(1), 144, 1977.

[Woh01] M. Wohlfahrt, *Untersuchung der dielektrischen Tieftemperaturanomalien von Mehrkomponentengläsern in Magnetfeldern*, Dissertation, Heidelberg University, 2001.

[Zac32] W. H. Zachariasen, The atomic arrangement in glass, *J. Am. Chem. Soc.*, **54**(10), 3841–3851, 1932.

[Zel71] R. C. Zeller and R. O. Pohl, Thermal conductivity and specific heat of noncrystalline solids, *Phys. Rev. B*, **4**(6), 2029, 1971.

[Zen32] Clarence Zener and Ralph Howard Fowler, Non-adiabatic crossing of energy levels, *Proc. R. Soc. London*, **137**(833), 696–702, 1932.

Acknowledgements

Meine Zeit in der Arbeitsgruppe hat mich sehr bereichert, besonderem Dank gilt hierbei

Prof. Dr. Christian Enss für die Möglichkeit Teil seiner Arbeitsgruppe sein zu dürfen in der ich herzlich aufgenommen wurde und viel gelernt habe,

Prof. Dr. Loredana Gastaldo für die Zweitkorrektur dieser Arbeit,

Dr. Andreas Reiser für die freundlichen Gespräche und die Korrektur dieser Arbeit,

Dr. Andreas Fleischmann für das tolle Low Temperature Physics Tutorium und das Näherbringen der mysteriösen Eigenschaften von Helium, welches mich so sehr beeindruckt hat, dass ich der Arbeitsgruppe beigetreten bin,

Christian Ständer für eine unglaubliche Betreuung und der Geduld bei all meinen Fragen und Anliegen, für die netten Gespräche und der detaillierten Korrektur dieser Arbeit,

meinen Büro Kolleg:innen Fabienne Bauer, Christopher Jakob, Pascal Willer und Alexander Stoll mit denen man immer quatschen kann wenn man mal eine Pause braucht,

Rudolf Eitel für die Versorgung mit flüssigem Helium,

Allen Mitgliedern der F3 und F4 für die freundliche Aufnahme, das angenehme Arbeitsklima und dem schönen Wanderausflug mit anschließendem Grillen,

den externen Korrekturlesern Philipp Zimmer, Christoph West und Alexander Slawik,

meiner Familie, die mich während meines Studiums immer unterstützt hat und meinen Freunden die die Zeit während meines Studiums unglaublich bereichern.

Ich versichere, dass ich diese Arbeit selbstständig verfasst und keine anderen als die angegebenen Quellen und Hilfsmittel benutzt habe.

Heidelberg, den 03.06.2022 .....

(Joyce Nicole Louisa Glass)